

Machine learning and marsquakes: a tool to predict atmospheric-seismic noise for the NASA InSight mission

A. E. Stott¹, R. F. Garcia¹, A. Chédozeau¹, A. Spiga², N. Murdoch¹, B. Pinot¹,
D. Mimoun¹, C. Charalambous³, A. Horleston⁴, S. D. King⁵, T. Kawamura⁶, N. Dahmen⁷, S. Barkaoui⁶,
P. Lognonné⁶, B. Banerdt⁸

¹ *Institut Supérieur de l'Aéronautique et de l'Espace SUPAERO, Toulouse, France.*

² *Laboratoire de Météorologie Dynamique/IPSL, Sorbonne Université, CNRS, Ecole Normale Supérieure, PSL Research University, Ecole Polytechnique, Paris, France*

³ *Department of Electrical and Electronic Engineering, Imperial College London, London, UK*

⁴ *School of Earth Sciences, University of Bristol, Bristol, UK*

⁵ *Department of Geosciences, Virginia Tech, Blacksburg, VA, USA*

⁶ *Université de Paris, Institut de physique du globe de Paris, CNRS, Paris, France*

⁷ *Institute of Geophysics, ETH Zurich, Zurich, Switzerland*

⁸ *Jet Propulsion Laboratory, California Institute of Technology, Pasadena, CA, USA*

Corresponding author email: Alexander.STOTT@isae-supero.fr

This manuscript is a preprint which has been submitted to Geophysical Journal International and has not yet been peer reviewed. Should the manuscript be accepted for publication a link to the final version will be available via the 'Peer-reviewed publication DOI' link. Note that any future versions of this manuscript may have slightly different content. Please feel free to contact the authors with any feedback.

SUMMARY

The SEIS experiment on the NASA InSight mission has catalogued hundreds of marsquakes so far. However, the detectability of these events is controlled by the weather which generates seismic noise. This affects the catalogue on both diurnal and seasonal scales. We propose to use machine learning methods to fit the wind, pressure and temperature data to the seismic energy recorded in the 0.4–1 Hz and 2.2–2.6 Hz bandwidths to examine low and high frequency event categories respectively. We implement gaussian process regression and neural network models for this task. This approach provides the relationship between the atmospheric state and seismic energy. The obtained seismic energy estimate is used to calculate signal to noise ratios (SNR) of marsquakes for multiple bandwidths. We can then demonstrate the presence of low frequency energy separate to the noise level during several events predominantly categorised as high frequency, suggesting a continuum in event spectra distribution. A method to detect marsquakes is implemented whereby a variable threshold is calculated for the subtraction of the predicted noise from the observed signal. This algorithm finds 32 previously undetected marsquakes, with another 34 possible candidates. Furthermore, an analysis of the detection algorithm’s variable threshold provides an empirical estimate of marsquake detectivity. This suggests that the largest events would be seen almost all the time, the median size event 45-50% of the time and smallest events 5-20% of the time.

Key words: Machine Learning – Planetary Interiors – Seismic Noise – Extraterrestrial seismology.

1 INTRODUCTION

The NASA InSight lander has recorded seismic and meteorological data for over three Earth years since arriving on Mars on the 26th of November 2018. This seismic data contains several marsquakes (InSight Marsquake Service 2022) which have enabled Stähler et al. (2021); Khan et al. (2021) and Knapmeyer-Endrun et al. (2021) to place constraints on the core, mantle and crust of Mars using seismological tools. The task of identifying marsquakes falls on the Marsquake Service (MQS) who systematically search the data as it is downlinked to identify marsquakes, as outlined in Clinton et al. (2021) and Ceylan et al. (2021). The first quake in the MQS catalogue is from sol 105, where a sol is a

Mars day and sol 0 is the landing day. Since then there have been 951 quakes in the \sim thousand sols of the mission so far. However, between sols 500 and 800 only 27 of these 951 events were observed. This is largely due to the environmental noise injection into the seismic data. The period corresponds to the northern hemisphere winter and is marked by the persistent presence of local turbulence throughout the Martian sol, characterised by Chatain et al. (2021). Moreover, even during the summer sols marsquakes are predominantly identified only in the quiet periods just after sunset when the weather conditions are extremely calm.

This demonstrates that atmospheric injection inhibits the discrimination of data of a seismic origin. In doing so, a complete catalogue of Martian events cannot be collated. This means events which would add further information on the Martian structure are missed and further constraints cannot be placed on the seismicity of Mars. Moreover, autocorrelation techniques have been implemented to examine the Martian structure. These approaches are either based on the coda of marsquakes or on identifying the ambient diffuse seismic wavefield (Compaire et al. 2021; Schimmel et al. 2021). As a result, the separation of the seismometer data into atmospherically induced and seismic origin components is of interest.

To limit atmospheric injection into the seismic data, the SEIS (seismic experiment for the interior structure of Mars) instrument was placed on the ground away from the lander and covered with a wind and thermal shield (WTS) (Lognonné et al. 2019). Stott et al. (2021) verified that the WTS removed the direct forcing pathway on SEIS and so reduced wind-induced signals. However, a problematic injection persists. The impact of wind, pressure and temperature on the seismic data was predicted in the pre-landing noise model of Mimoun et al. (2017). At the lowest frequencies $< 1e - 3$ Hz temperature effects dominate (Lognonné et al. 2020). Garcia et al. (2020) showed pressure coupling through compliance for certain periods of the sol below 0.5 Hz. For marsquakes however, wind noise dominates, with the lander providing a key source of vibrations as outlined in Murdoch et al. (2017, 2018); Stott et al. (2021). The in situ sensitivity of the seismic data to the wind and pressure variation was examined in Charalambous et al. (2021), which described the relationship between the seismic energy level (i.e. envelope of the seismic data), wind speed and pressure fluctuations.

Atmospherically generated noise, therefore, forms the most significant component of seismic noise on Mars. Machine learning has been applied to separate such noise features within seismic data on Earth, for example, in Johnson et al. (2020) and Seydoux et al. (2020). These unsupervised learning approaches aim to cluster data segments with common attributes. The deep scattering network approach in Seydoux et al. (2020) was implemented for the InSight data in Barkaoui et al. (2021), which identified types of glitches (Scholz et al. 2020) and atmospheric noise. In planetary scenarios, machine learning approaches have been applied for event detection on the Moon. Knapmeyer-Endrun

& Hammer (2015) and Civilini et al. (2021) respectively developed a hidden markov model and convolutional neural network approach to detect patterns related to moonquakes. These are a supervised learning classification style problem.

The aim of this work is to analyse the seismic data, and therefore marsquakes, with respect to the atmospheric contribution. To that end, we formulate a supervised learning regression style problem, to predict the seismic energy from the atmospheric data. This integrates the wind speed, wind direction, pressure and temperature data to allow for information on the variability in the relationship due to atmospheric conditions to be taken into account. We implement two types of machine learning algorithms for this curve fitting task, gaussian process (GP) regression and a multilayer perceptron (MLP) neural network (NN). The resulting machine learning models produce an estimation of the atmospheric noise level in the SEIS data. This prediction can be used as a tool to analyse known marsquakes and identify new ones.

2 DATA AND PREPROCESSING

2.1 The Seismic data

The InSight events are catalogued by the marsquake service according to a developed taxonomy. The event categories (as described in Clinton et al. (2021)) are split as:

- Low frequency (LF) - energy below 2.4Hz on all three components
- Broadband (BB) - energy predominantly below 2.4Hz on all three components with some excitation above and including the 2.4Hz mode.
 - 2.4 Hz - energy in all three components localised to the 2.4Hz mode.
 - High frequency (HF) - energy in all three components predominantly at 2.4Hz and above.
 - Very high frequency (VF) - energy in all three components predominantly at 2.4Hz and above but the horizontal energy is greater than the vertical for higher frequencies. They have a particular spectral characteristic.
- Super high frequency (SF) - very short duration, exciting energy above 2.4Hz with horizontal energy larger than vertical.

The 2.4Hz mode is proposed to be a resonance of geophysical origin and is excited by seismic events at these frequencies (Dahmen et al. 2021b; Giardini et al. 2020; Hobiger et al. 2021; Compaire et al. 2021). On top of event excitation it is also observed ambiently (Dahmen et al. 2021b; Compaire et al. 2021) with a variable amplitude when the noise level is low enough.

For our purposes we can split them into a lower frequency (LF and BB events) and higher frequency category (2.4 Hz, HF and VF events). In this work we do not examine the SF events as these

are already detected by an automated algorithm (Dahmen et al. 2021a). On top of these categories, the events are split into the following classes:

- A - multiple clear phases with clear polarisation
- B - multiple clear phases with no polarisation or with polarisation but not clearly identifiable phases
- C - signal is clear but clear phase picking is difficult
- D - signal is very weak, impossible to pick phases or may not be a seismic event.

As described in Clinton et al. (2021). The aim of this class system is to indicate their usability for seismic analysis, as much as their general quality.

Figure 1 shows the probabilistic power spectral density (PPSD) of the VBB (the very broadband seismometer on SEIS) data taken over sols 257–267. This is the histogram of the PSD over this period and is normalised to give the probability of the PSD taking that value for a given frequency. To examine the lower frequency group we use the velocity channel filtered between 0.4-1 Hz. This region has a relatively flat/white spectrum as shown in Figure 1.

For the higher frequency category we focus on the 2.2-2.6Hz range to isolate the energy in the 2.4 Hz mode, which is always excited by events in this group. Isolating this mode means that we do not have to be concerned with the increasing sensitivity to wind with increasing frequency, shown in Figure 1.

2.2 Preprocessing and data cleaning

Based on the above considerations for how atmospheric energy can generate seismic signals, the data used for the machine learning models are:

- Seismic energy level of the VBB Z,N and E axes
- wind speed boom 1 and 2
- wind direction boom 1 and boom 2
- air temperature from boom 1 and boom 2
- pressure and its envelope

Note boom 1 and 2 refers to the two different wind sensors of TWINS, which each have complementary orientations designed to cover wind from all directions (Banfield et al. 2019). The machine learning model therefore has eight inputs (2 wind speeds, 2 wind directions, 2 air temperatures, the static pressure and the RMS envelope of the pressure signal) and three outputs (the seismic energy level, envelope, for Z, N and E).

Prior to the implementation of machine learning algorithms, the InSight data must be pre-processed

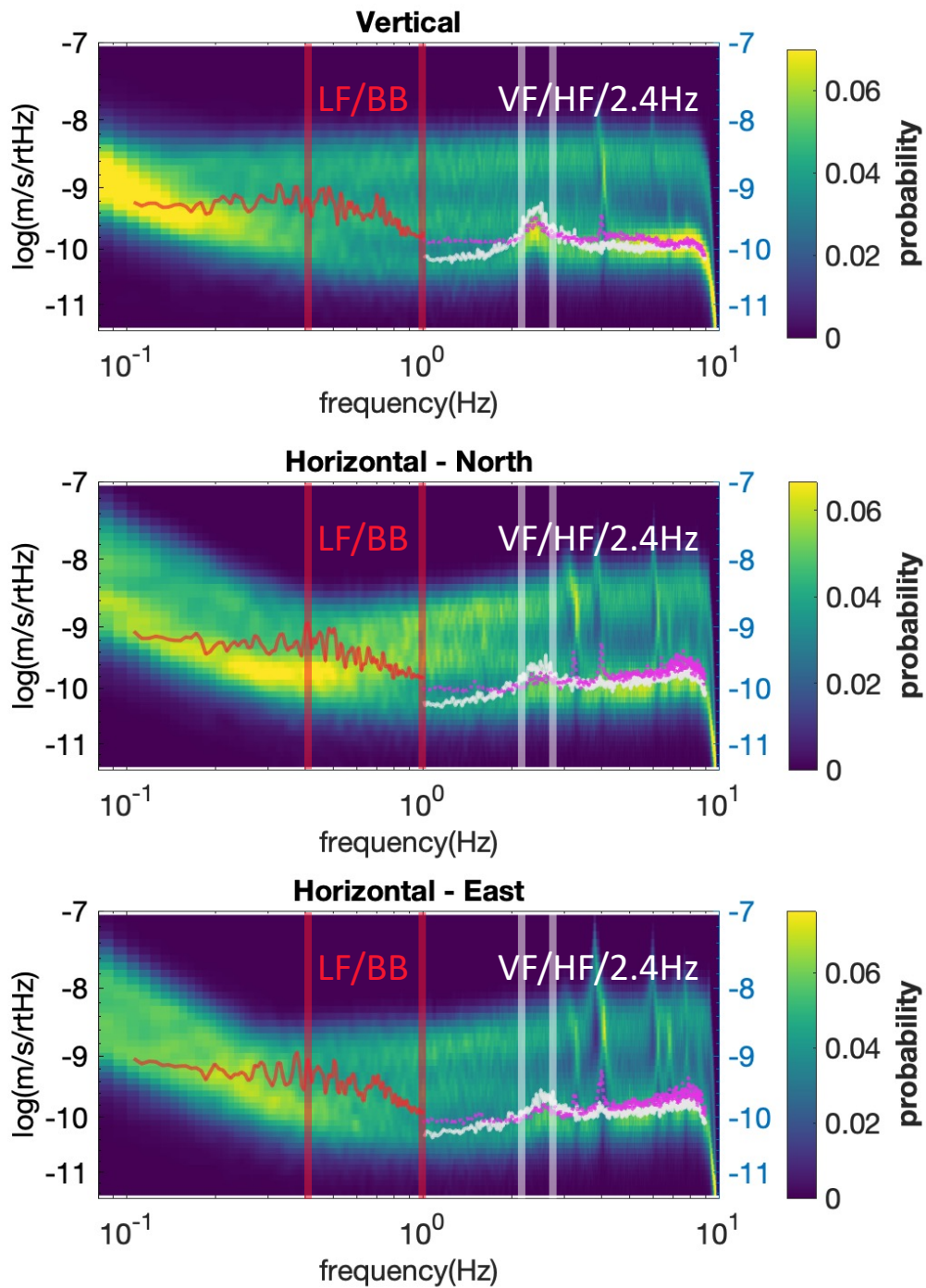


Figure 1. The PPSD of the (top to bottom) vertical, north and east components of the VBB over sols 257–267. The red PSD overlay is the LF S0173a event, the white is the HF S0424c and the magenta is the VF S0475a event. The red lines indicate the 0.4–1Hz band used for the low frequency envelope and the white lines the 2.2–2.6Hz bandwidth for the high frequency envelope.

and cleaned. InSight data are available (both seismic and meteorological) in miniseed (Service 2019). We use the ObsPy Python package (see Beyreuther et al. (2010); Megies et al. (2011); Krischer et al. (2015)) for processing the data.

There are several data issues and peculiarities that need to be taken into account. For example, the data available for each sensor over the mission are not always at the same data rate, due to data downlink volume considerations. Moreover, there are periods of data dropout on some sensors either from anomalies or, more recently, power considerations when some sensors had to be turned off. The preprocessing must blend together this data taken at different sampling rates and identify the periods when data from all sensors was available. The data channels used are outlined in Table A1.

The first step is to identify the sols which have coincident data from all sensors, that is, find the sols where there is at least one of the channels in Table A1 for each sensor. Once this has been obtained, the seismic data pipeline is to:

- Load data
- remove the sensor response
- rotate to the vertical (Z), north (N) and east (E) coordinate frame
- filter to 0.4–1 Hz and 2.2–2.6 Hz bandwidth
- compute the signal envelope over 10s
- downsample to 1 sample per second (sps)

The pressure data is similarly filtered to obtain the envelope and both the envelope and original data are downsampled to 1 sps. The wind speed, direction and air temperature are also converted to the common sample rate of 1 sps, which is chosen as it is the most common sample rate for this data. Each data vector is saved sol by sol so that the processing can be done in batches and is readily extended to new data.

After this initial treatment, several artifacts must be removed from the data. These include:

- Large erroneous peaks
- Other peaks due to glitches and other transients
- Data gaps

The glitches are a common problem to tackle with the InSight seismic data and most are removed through the ISAE deglitching technique proposed in Scholz et al. (2020). However, some remain which appear as spikes in the envelope. A further processing step is made to remove these peaks significantly above the local median value of the data within a window. The data gaps are identified from the miniseed files. The method to discount these periods of data is through a mask vector, which

is a Boolean logical inclusion or exclusion of the data at that point. This makes it straightforward to modify without deletion and manipulate the data, in terms of keeping the original time sample.

The next step is to apply the transformations for input into the machine learning algorithms. The seismic envelope is converted to its base 10 logarithm to give the seismic energy level and, along with the pressure envelope, is smoothed with a moving mean and median filter each of length 15s. Then each variable is normalised to have an amplitude between -1 and 1. The final data is stored along with the mask vectors for each sol. After this full pre-processing, ~ 30 million samples are available (at 1 sps up to sol 1000) for use with the machine learning algorithms.

In order to handle the large memory and computational requirement for both the pre-processing and training machine learning models the code was run on the CALMIP computing cluster facility. The choice to operate on the data one sol at a time when possible enabled parallelisation of the code for improved calculation time and reduced the need for very large matrices to be stored or operated on.

3 ATMOSPHERICALLY GENERATED NOISE

Prior to landing, Mimoun et al. (2017) constructed a noise model for SEIS to determine the level of injection from each possible noise source. In the bandwidths where seismic events are observed, the main effect is due to the wind. The forcing mechanism is given by drag/lift

$$F = \frac{1}{2} C_{D/L} A \rho_A U^2 \quad (1)$$

where $C_{D/L}$ and A are the drag/lift coefficient and surface area of whichever body the wind forces, ρ_A is the air density and U the wind speed.

The pathways through which this will generate vibrations sensed by SEIS are either by forcing on the lander or on the WTS, whereby the vibrations are coupled through the regolith to SEIS feet. Murdoch et al. (2017) developed a physical model for lander-induced vibrations into the SEIS data which was integrated into the overall noise model of Mimoun et al. (2017). Stott et al. (2021) verified that lander-induced vibrations are the dominant noise source at least for high wind speeds. The lander and SEIS assembly also have vibrational modes excited by the wind which were modelled in Murdoch et al. (2018) and analysed in Dahmen et al. (2021b); Hurst et al. (2021).

On top of wind-induced sources, pressure forcing can cause ground deformation (Garcia et al. 2020; Kenda et al. 2020). Moreover, Charalambous et al. (2021) demonstrated that the pressure envelope between 0.1 and 4 Hz is well correlated to the seismic energy level. The VBB is also directly sensitive to temperature (Mimoun et al. 2017), however, this does not fluctuate on the scale of events so we only consider the atmospheric temperature to take into account changes of air density. The mag-

netic field variations so far have not been seen to be very well correlated with the seismic data in event bandwidths and so are not included.

3.1 The variation of the atmospheric data with the seismic data

The input-output relationships for the preprocessed data are shown in Figure 2 for three periods (of three sols) over the mission centred around sol 258, 495 and 690. The colour coding indicates the time of the sol where dark colours indicate night, turning progressively lighter through blue during the morning and then darker through red in the afternoon to the night. It can be seen that the relationship between the seismic data and each of these variables changes over both the Martian sol and season, as was demonstrated in Charalambous et al. (2021). This is straightforwardly observed by the variation with pressure in Figure 2, which covers a different range for each section. In short, the goal of the machine learning is to fit the curves presented in Figure 2, accounting for both diurnal and seasonal variation.

Now, over a Martian year of coincident seismic and atmospheric data is available to further determine the sensitivity over seasons. Some cause of this variability can be understood through consideration of the drag/lift equation 1. First of all, this is dependent on the air density which is, in turn, dependent on pressure and air temperature. Moreover, drag/lift coefficient is dependent on the atmospheric conditions, for example, whether the wind is in a turbulent or laminar flow. As a result, we must consider the atmospheric stability at InSight over the Martian day and seasons, presented in Spiga et al. (2021); Banfield et al. (2020) and Chatain et al. (2021).

During the daytime on Mars there is strongly convective turbulence. This provides the highest wind speeds and strongest seismic response. On the other hand, the night time turbulence is generally weaker and the Martian atmosphere is more stably stratified. Although the night time signals are not usually as strong as the daytime, the seismic response is more sensitive meaning there is a higher velocity for a given wind speed than during the day, as shown in Figure 2 where the darker colours at night generally show a steeper slope to the wind speed than the lighter daytime colours. There can also be a quiet period just after sunset when the planetary boundary layer collapses and there is little wind speed. During this period there is very little wind or turbulence and so this period is where most seismic events are found (Clinton et al. 2021).

Chatain et al. (2021) investigated the seasonal variability in turbulence across the Martian sol at InSight. They showed that a buoyancy source is the dominant factor for the daytime turbulence whereas the evening/night time turbulence is driven by wind shear. Earlier in the mission, the stable atmosphere at night also creates a buoyancy sink which can inhibit the shear source, causing a turbulent flow to move towards a laminar one. As the northern hemisphere winter approached, the wind shear

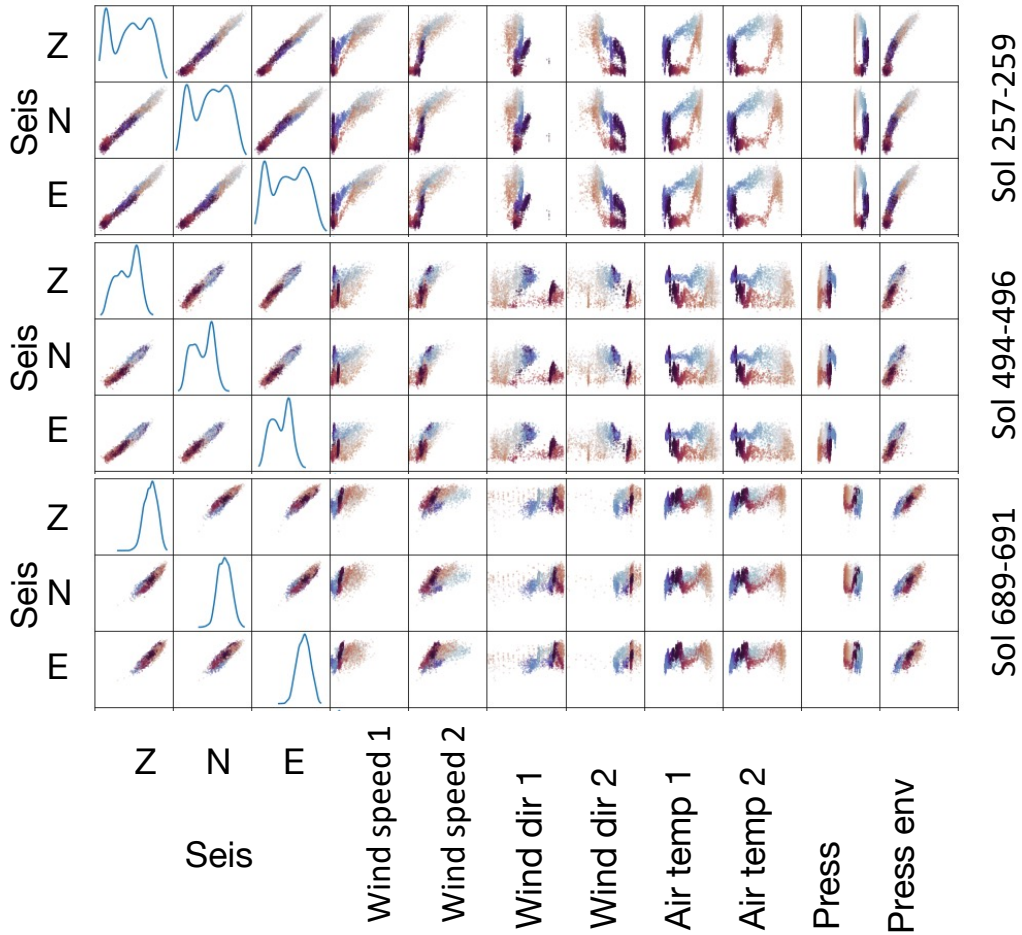


Figure 2. A matrix of scatter plots between the atmospheric data (model inputs) and the three axis seismic noise levels (model outputs). This is plotted for 3 sols at 3 different seasons over the mission. The diagonal is the kernel density estimate (KDE) of the probability density function (pdf) for the seismic data. The colour indicates the time of the sol starting with black at midnight LMST (local mean solar time) going to lighter blue to midday before turning darker red over the afternoon.

source begins to dominate the buoyancy sink, leading to increased evening/night time turbulence and the quiet period completely disappears.

The evolution of the effects of the turbulence with respect to the seismic data is exhibited in Figure 2. First consider the KDE (kernel density estimate) probability density function (PDF) estimate for each of the seismic axes. For the sol 258 section, there are three modes and a wider range covered. In the sol 495 section the range narrows and there are two modes before a single mode is shown in the sol 690 section. The three modes are consistent with the distinct appearance of daytime convective turbulence, nighttime/early morning turbulence and the quiet period. These distinctions slowly disappear until the sol 690 season where there is turbulence throughout the day, as described above. This is

matched by the relationships to each of the atmospheric data, which generally appear to collapse and become less structured as the conditions are more similar diurnally. However, the different regimes are still separable. For example, in the sol 690 section the dark nighttime zone in the wind speed boom 2 and pressure envelope is still distinct from the other times of sol. The slope is still greater than for the other times of sol but shallower than the same coloured zone in the other seasons. This matches the analysis of Chatain et al. (2021).

Although the seismic response is understandable in terms of the physical relationship, it also illuminates that there are many components to take into consideration. As a result, it is difficult to determine a physical model which is able to predict the seismic signal sufficiently for event analysis. To that end, we implement a machine learning model to account for the complexities outlined here. This also allows other possible sources/forcing to play a part in the prediction, which may not be immediately identifiable.

4 IMPLEMENTATION OF THE MACHINE LEARNING MODELS

The next step is to implement machine learning models to fit the input-output relationships demonstrated above in Figure 2. The atmospheric variables (the 2 wind speeds, directions, air temperatures, pressure and pressure envelope) are the inputs and the envelope of the three seismometer axes are the outputs. We consider two main methods to do this, gaussian process regression and neural networks. At a base level each of these approaches can be considered equivalent implementations to obtain the prediction. We will first present their individual applications to the data and then compare their performances.

4.1 Gaussian process regression

4.1.1 Background

A Gaussian process, as defined in (Williams & Rasmussen 2006), is a set of random variables where any finite selection has a joint Gaussian distribution. Gaussian process regression applies this probabilistic approach around the regression model

$$y = f(\mathbf{x}) + \eta \quad (2)$$

where the output of the model y is predicted from the input vector \mathbf{x} through the function $f(\cdot)$ plus some white noise $\eta \sim \mathcal{N}(0, \sigma^2)$. The function $f(\cdot)$ is considered to be gaussianly distributed itself, that is, we consider the distribution of functions that fit the data. In this way Gaussian process regres-

sion is considered non-parametric, as opposed to having a specific form defined by parameters, e.g. a quadratic function.

In the Gaussian process framework the distribution of the function is given as

$$f(\mathbf{x}) \sim \mathcal{GP}(m(\mathbf{x}), k(\mathbf{x}, \mathbf{x}')) \quad (3)$$

where $m(\mathbf{x})$ and $k(\mathbf{x})$ are termed the mean and covariance function of the output $f(\mathbf{x})$. These functions are selected depending on the characteristics of the problem at hand. The mean function can be used to encode known functional information directly. The covariance function sets the prior form for the functions that fit the data, that is, it determines the characteristics of the functions that fit the data. The covariance function must be positive-semidefinite and is described by a chosen kernel function to give the level of similarity between the outputs for two arbitrary inputs \mathbf{x} and \mathbf{x}' .

From the definition, any set of samples from a gaussian process has a multivariate normal distribution. So for a set of inputs, $\mathbf{x}_1, \dots, \mathbf{x}_n$, denoted as X the vector of function outputs $\mathbf{f} = [f(\mathbf{x}_1), \dots, f(\mathbf{x}_n)]$ has the distribution

$$\mathbf{f} \sim \mathcal{N}(\mathbf{m}, \mathbf{K}) \quad (4)$$

where $\mathbf{m} = [m(\mathbf{x}_1), \dots, m(\mathbf{x}_n)]$ and the matrix \mathbf{K} has entries $k_{ij} = k(\mathbf{x}_i, \mathbf{x}_j)$. For simplicity the mean is herein set to be zero. Now consider the set of inputs X along with the corresponding outputs \mathbf{y} . To train the gaussian process regression model we must obtain the conditional distribution (the posterior) as

$$\mathbf{f}|X, \mathbf{y} \quad (5)$$

For a set of new, test inputs, denoted as X^* , the prediction from the gaussian process regression can be inferred from the conditional distribution

$$\mathbf{f}|X, \mathbf{y} X^* \quad (6)$$

where the joint distribution of the vectors \mathbf{f} and \mathbf{f}^* follows the multivariate normal distribution. This can be evaluated assuming the white gaussian noise term η . Note that this is a distribution and so the prediction is taken as the expectation. The covariance can also be extracted and so the evaluation of prediction confidence intervals is straightforward.

The performance of a gaussian process regression model depends on the selection of the mean and covariance functions, that is, the prior distribution of the function. The mean function is usually set to zero. The covariance function is often set by a kernel.

The behaviour kernel and mean functions are controlled by hyperparameters. For example, a com-

mon kernel function is the squared exponential

$$k(\mathbf{x}, \mathbf{x}') = \exp\left(-\frac{|\mathbf{x} - \mathbf{x}'|^2}{2l^2}\right) \quad (7)$$

where the lengthscale hyperparameter l defines the level of similarity between two points at a distance $|\mathbf{x} - \mathbf{x}'|$. To evaluate the appropriate hyperparameter value for a given problem an optimisation is performed to maximise the log marginal likelihood of the training data given as

$$\log(P(\mathbf{y}|X)) \quad (8)$$

In this work we use the GPy library for Python (GPy since 2012) to implement gaussian process regression models. The prediction requires matrix inversion and so has high computational complexity. This makes them more appropriate for small datasets.

4.1.2 Implementation

A global model was fitted using 3000 data samples for the training data, randomly selected from across the entire data available. The prediction of this model was then calculated for each sol separately and stored. Four models with different kernels were trained on the LF data to identify the best choice. These were 1) an Exponential kernel, 2) radial basis function (RBF), 3) Exponential added to a Multilayer Perceptron (MLP) kernel and 4) Exponential added to an MLP kernel multiplied by another exponential kernel. For further details on these kernels see Williams & Rasmussen (2006).

To evaluate model performance we use the root mean square error (RMSE) metric given by

$$RMSE = \sqrt{\frac{1}{N} \sum_{n=0}^{N-1} (y_n - \hat{y}_n)^2}$$

where N is the number of data points, y_n and \hat{y}_n are the observed and predicted values at time instance n . The RMSE was calculated on 20% of the whole mission's data (test data not used for training) for each model and is shown in Table 1. The Exponential + MLP kernel marginally the lowest error and so was selected for use in the rest of this study.

This global model used only 3000 samples to calculate the fit, which is a very small portion of the total ~ 30 million available. This is because gaussian process regression requires significant computational and memory resources in optimisation and prediction. As a result, using a larger portion of the data for training quickly becomes intractable. This global model provides a good estimate of the relationship dynamics, however, it may not sufficiently represent some parts of the atmospheric-seismic relationship for marsquake analysis. To this end, we also propose a local model where a gaussian process regression model is obtained independently for each sol. The training data for this model are 3000 samples randomly selected from the preceding and following sols. In this way, the

GP Kernel type	Test RMSE
Exp.	0.075
RBF	0.078
Exp. + MLP	0.074
Exp. + MLP \times Exp.	0.075

Table 1. RMSE of GP global model for different kernels

local conditions are best accounted for. This local method does require significantly more resources as a new model is trained for each sol, when only one for the entire mission was previously required. Herein we will refer to the GP model trained on data sampled from across the entire mission as the global GP model and the GP trained on data only from the surrounding sols as the local GP model.

4.2 Neural Networks

4.2.1 Background

A neural network takes each element in an input feature vector and maps them to an output value through a series of connected "neurons". Each "neuron" multiplies each connection by a weight before summing, applying a bias (also a type of weight) and passing through an activation function (Murphy 2012). The activation function can take several forms, for example the ReLu (rectified linear) function given as

$$f(x) = \max(0, x) \quad (9)$$

where the output is zero for inputs below zero and linear for outputs above. This choice is useful for regression problems and is less susceptible to vanishing gradient problems than other activation function choices (Goodfellow et al. 2016). The full neural network is made up of sequentially applied layers each consisting of several neurons taking the output of the previous layer as an input until the output layer is reached.

The number of neurons in each layer is the breadth of the network and the number of layers is the depth. Large numbers of layers gives rise to deep learning (Goodfellow et al. 2016), useful for approximating extremely complex functions. Neural networks are able to approximate a wide class of functions (universal approximation theory (Cybenko 1989)) given an appropriate architecture, that is, the choice of activation functions, number of layers and number of neurons on each layer. These are determined through tuning, whereby several networks of different topologies are trained and then evaluated on test data (data not used to train the neural network) to determine overfitting. The model which achieves the best performance on the test data is selected as the appropriate architecture.

The training of a neural network to a specific task requires the weights and bias values for each neuron to be optimised. This is achieved through stochastic gradient descent algorithms to find the minimum of the loss function, in our case the mean square error of the predicted output and the target output. These algorithms evaluate the gradient (using back-propagation) for a sample of training data and iteratively update the weights to step towards the minimum of the loss function. The step size is controlled by a learning rate, trading off eventual accuracy and convergence speed. A detailed explanation can be found in Murphy (2012) and Goodfellow et al. (2016) for example.

A complete pass of the training data is known as a training epoch. Several epochs may be completed to finalise the model weights. The loss error must, however, be evaluated on a test set of data to verify that each new epoch is improving the performance and not overfitting. As very large datasets can be used for training, it may be required to split it into batches for computational efficiency. In this case the algorithm iterates across each batch until the epoch is completed where the process is terminated or continued for further epochs. In general, the neural network performance improves for larger datasets.

4.2.2 Implementation

A multilayer perceptron neural network architecture was implemented using the Keras python package of Chollet et al. (2015). Each neuron was defined by the ReLU activation function in equation 9, apart from the final output layer where a linear combination was used. The training dataset was 80% of the entire data available selected at random with the remaining 20% used to evaluate the model performance and detect overfitting.

The required number of layers and neurons in each layer for a given task were selected by finding the level of model complexity beyond which little improvement can be made or overfitting occurs. Figure 3 shows the test and training error for a range of models. None show a significant increase in error between the testing and training data sets, that is, no model clearly overfits the training data. This can occur when the training data are very numerous compared to the number of parameters in the network. The large dataset means that the input-output relationship is fully explored and a new observation point is unlikely to be found. The selected model for analysis has 6 layers with 20 neurons on each layer. This was chosen as there is little improvement in a more complex model.

The training for each model used the ADAM optimiser (Kingma & Ba 2014) (a variant of the stochastic gradient descent algorithm) with a starting learning rate of 0.001 and done over 100 epochs. Figure 4 shows the training and test error over these epochs. The test loss is fluctuating around the training loss but follows its trend, indicating there is no overfitting. The loss change is at an al-

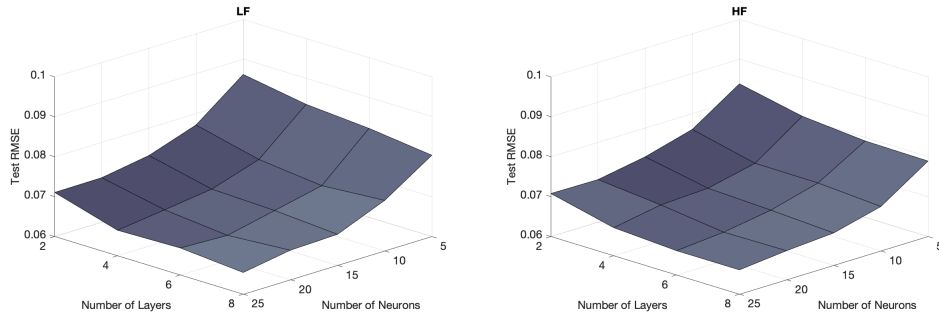


Figure 3. The test data RMSE for neural networks with different numbers of layers and neurons per layer.

most steady state and so the training is complete. The model used for the results is referred to as the NN/neural network model.

4.3 Analysis of the fits

In this section we will discuss the performance of the GP and NN models trained above to predict both the LF (0.1-1Hz) and HF (2.2-2.6Hz) seismic energy. Table 2 shows the RMSE computed for each of the three models from 20% of the overall data. This gives a comparable view of the overall performance for each model. The neural network approach provides the lowest error, followed by the local and then global GP models. This is the case for both LF and HF seismic energy predictions, while the LF has slightly better performance than the HF. For the local GP model, several sols were removed from the error calculation as they had erroneous predictions due to sampling data artifacts in the training data.

In order to analyse how the performance of models varies over the Martian sol and seasons we

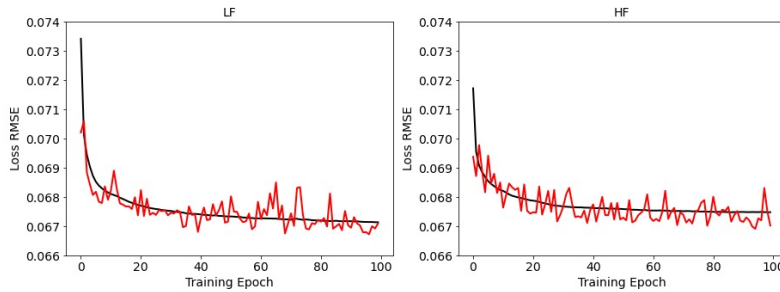


Figure 4. The test and training RMSE of the neural networks models for LF and HF over 100 training epochs.

Model	Test RMSE	
	LF	HF
GP global	0.074	0.081
GP local	0.072	0.075
Neural network	0.067	0.067

Table 2. RMSE of ML models

will examine over three exemplar sols: 258, 495 and 690. For the LF bandwidth, Figures 5, 6 and 7 show the predictions compared to the observations and residual errors of the LF bandwidth for the GP global, GP local and neural network respectively, while Figures 8, 9 and 10 show the same for the HF bandwidth. The residuals are shaded with their smoothed values over 100s and 1000s and their pdf estimates are shown on the side panel. First notice that there is no significant difference in the prediction of the vertical (Z) and horizontal (N and E) components for any model and for all sols. Table 3 shows the RMSE for each sol for each model. For each sol the RMSE is lowest for the neural network, followed by the local GP and then global GP, as was the case with the error calculated over the whole dataset. This is aside from the local prediction on sol 690 where the local GP has equivalent/slightly improved error than the neural network for the LF and HF predictions respectively.

On Sol 258 there are three clear regimes: daytime turbulence, the evening quiet period and night time turbulence. These regimes change over the mission, most notably the quiet period is only briefly visible on sol 495 and has disappeared by sol 690, when the night time turbulence has become more intense. The pdf of the residuals is generally gaussian-like and consistent for each sol, indicating there is no major change in the prediction quality over the seasons. However, certain features can be noticed. The night time (turning into early morning) turbulence shows sharp transient level changes, especially on sol 258 and sol 690. These rapid transient shifts are not always instantly predicted and cause a level change in the residuals highlighted by the light coloured smoothed trends. As mentioned these level changes do not occur uniformly on each sol and are due to variation in the atmosphere. The cause of error may indicate that the seismometer is adapting quicker the environmental change than

Model	Sol 258		Sol 495		Sol 690	
	LF	HF	LF	HF	LF	HF
GP global	0.068	0.077	0.077	0.078	0.70	0.077
GP local	0.066	0.075	0.074	0.074	0.064	0.068
Neural network	0.064	0.071	0.069	0.070	0.064	0.069

Table 3. RMSE of ML models for three sols

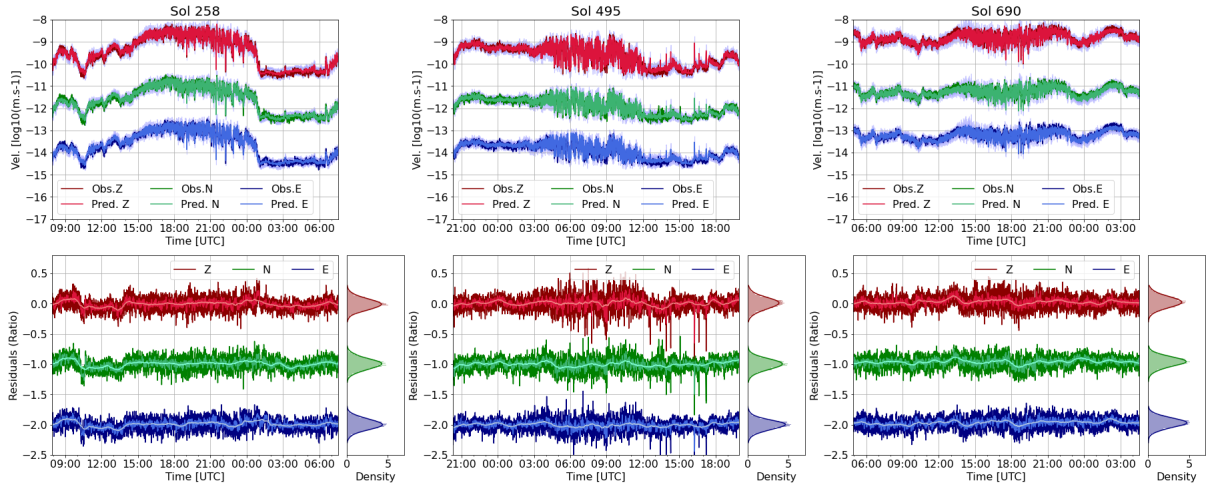


Figure 5. Global GP LF prediction and observations

the atmospheric sensors. Moreover, the daytime convective turbulence has greater variation than the other turbulent periods. This variation is largest on sol 495, where the residuals are larger during the daytime and so their distribution is not completely stationary. Note that sol 495 also has the largest RMSE for the LF prediction.

The prediction of the HF energy level during the quiet, low noise, periods is generally more constant in appearance than for the LF. This suggests that the HF estimates do not predict all the general level variation in this regime. This is the likely cause of the higher RMSE generally seen for the HF compared to the LF predictions. One possible reason is that the atmospheric sensors are not sensitive enough for this prediction, as the higher frequencies are generally more sensitive to the wind (Charalambous et al. 2021). On the other hand, the HF prediction covers the 2.4Hz mode. As introduced,

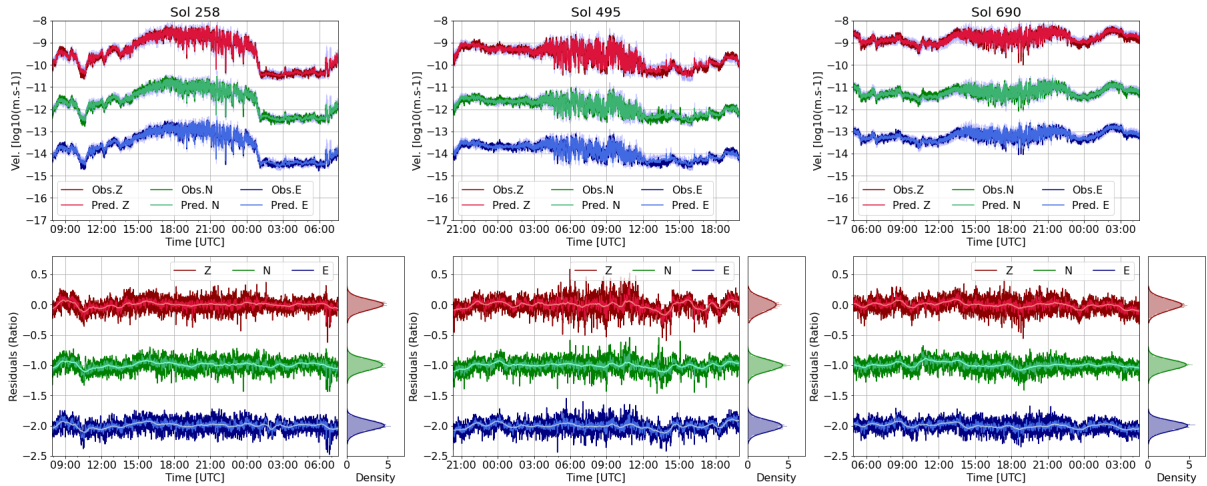


Figure 6. Local GP LF prediction and observations

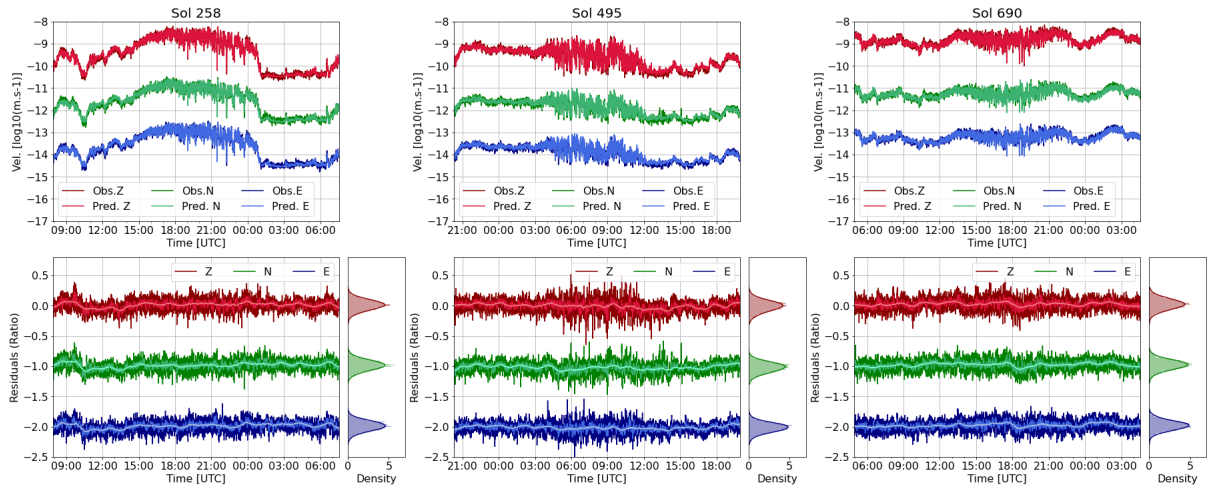


Figure 7. NN LF prediction and observations

this mode is proposed to be of geophysical origin and amplifies events in this bandwidth. However, the mode also exhibits ambient modulation, the origins of which have yet to be pinned down. The fact that these machine learning models fail to predict the overall ambient variation of the 2.4Hz suggests that it is not generated with local atmospheric effects. The 2.4Hz mode is only directly observed when the noise is low enough, for example during the quiet periods. A quiet period is only seen on sol 258 and 495. As a result, this effect explains the slightly lower RMSE for the HF sol 690 prediction.

One major advantage of the GP models over the neural networks is that the prediction is given as a distribution, and so confidence intervals are obtained intrinsically. These confidence intervals (plotted at 95%) are generally much tighter to the prediction for the local GP than the global GP model, indicating the local model to have better constrained the relationship.

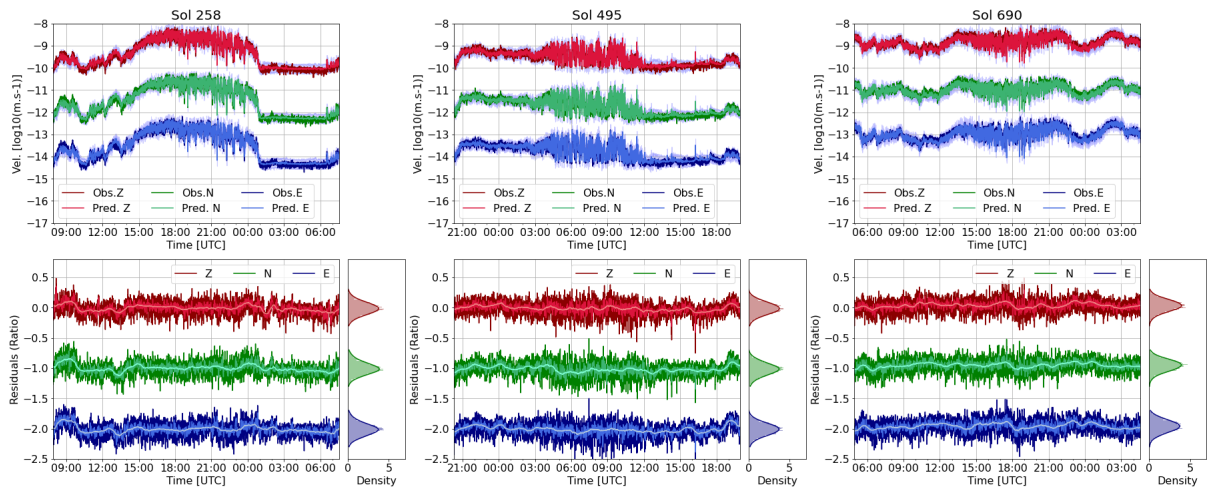


Figure 8. Global GP HF prediction and observations

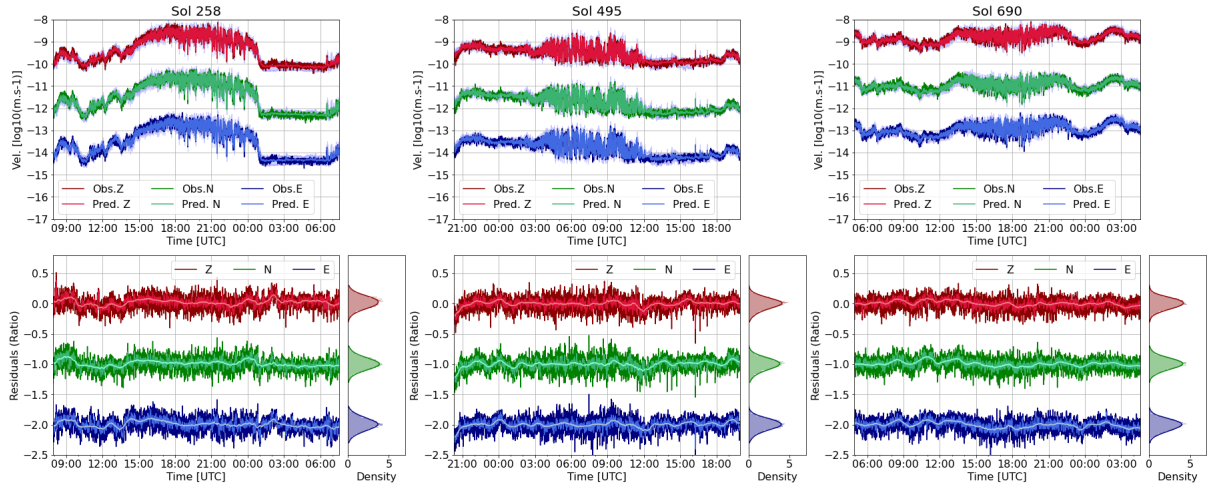


Figure 9. Local GP HF prediction and observations

5 QUAKE ANALYSIS AND DETECTION

In this section we take the seismic noise energy predictions/estimates of the introduced machine learning models and show how we can use it to examine the quality of and detect events. The best performing and most robust model is that of the neural network and so we will use its results unless stated otherwise.

5.1 Signal to noise ratio of marsquakes

The prediction residual indicates the seismic signals independence from atmospheric injections. As the subtraction is in the logarithmic domain, the residual is in fact, the signal to noise ratio (SNR) of the observed energy to the predicted noise level. We calculate the SNR for a particular event is

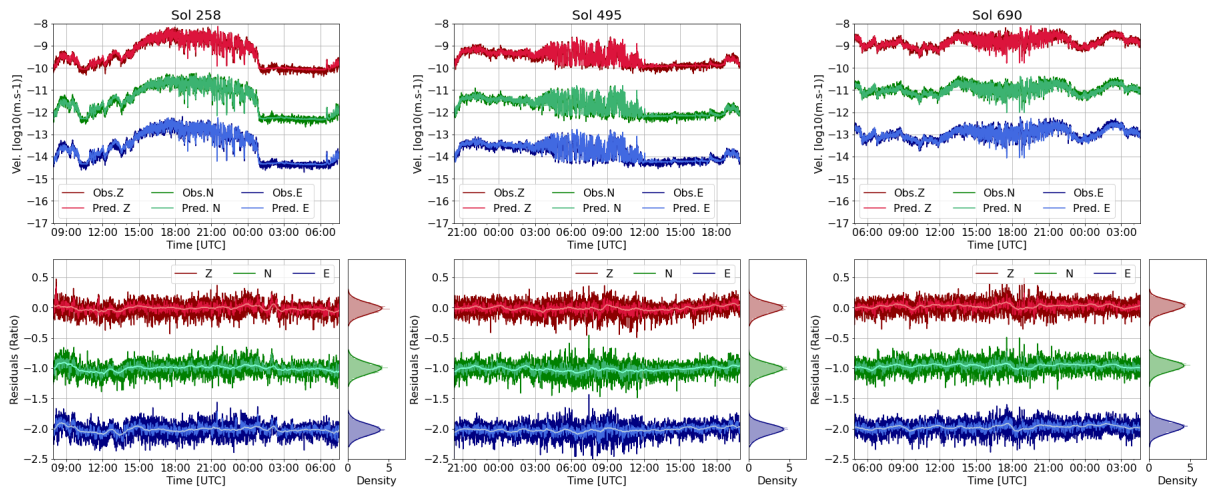


Figure 10. NN HF prediction and observations

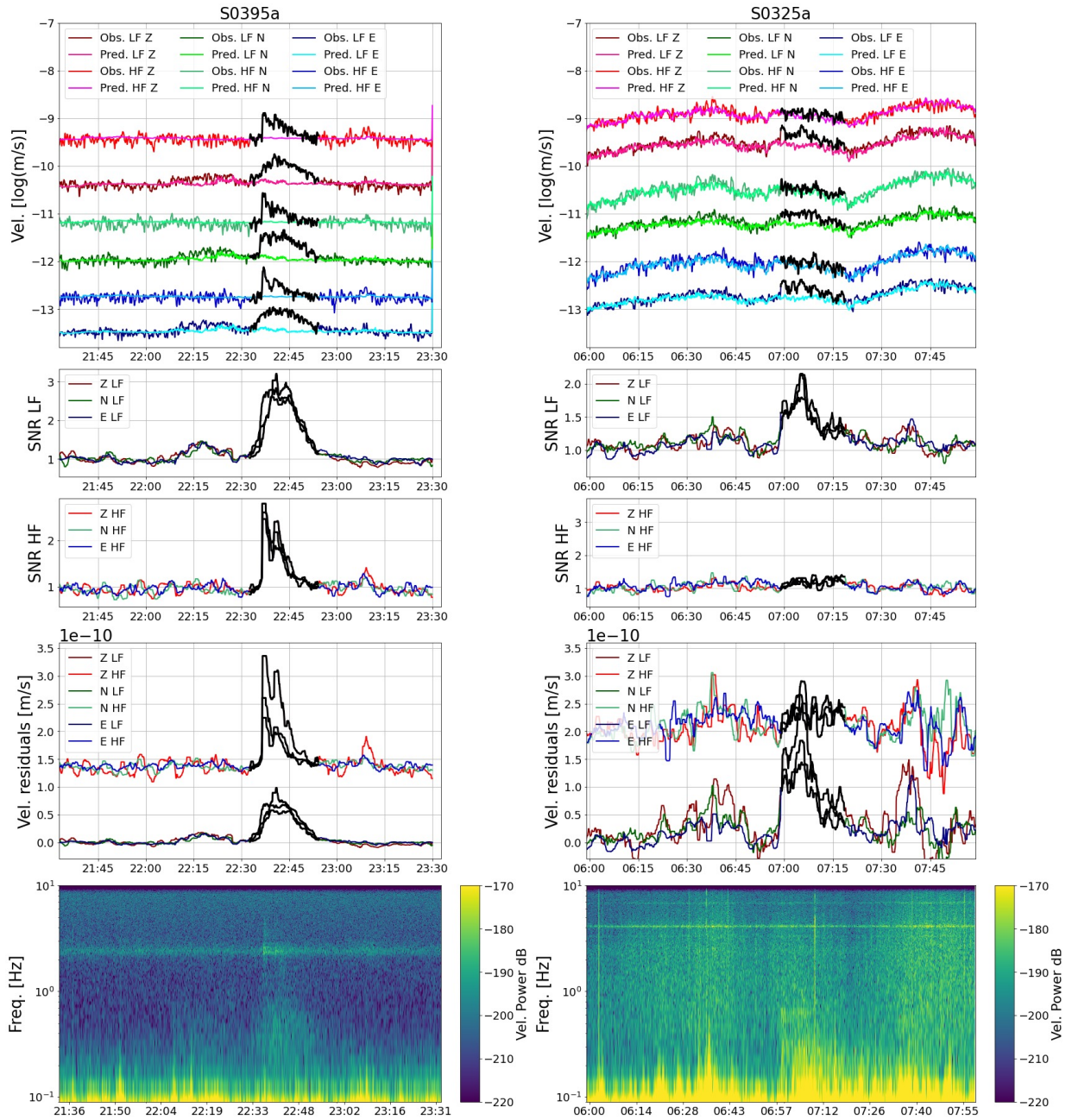


Figure 11. The NN model predictions and SNR analysis for the S0395a BB quality C and S0325a LF quality B events.

given as the maximum of this residual signal during the event, based on the prediction from neural networks. This SNR has been calculated for every event (with available data) in the catalogue in both the low frequency (0.4-1 Hz) and high frequency (2.2-2.6 Hz) bandwidths, a table of these are given in Appendix C. Note that this SNR is in terms of signal energy.

Figure 11 shows two low frequency type events, S0395a a BB quality C S0325a an LF quality B. The observed seismic energy during both events clearly deviates from the predicted noise levels

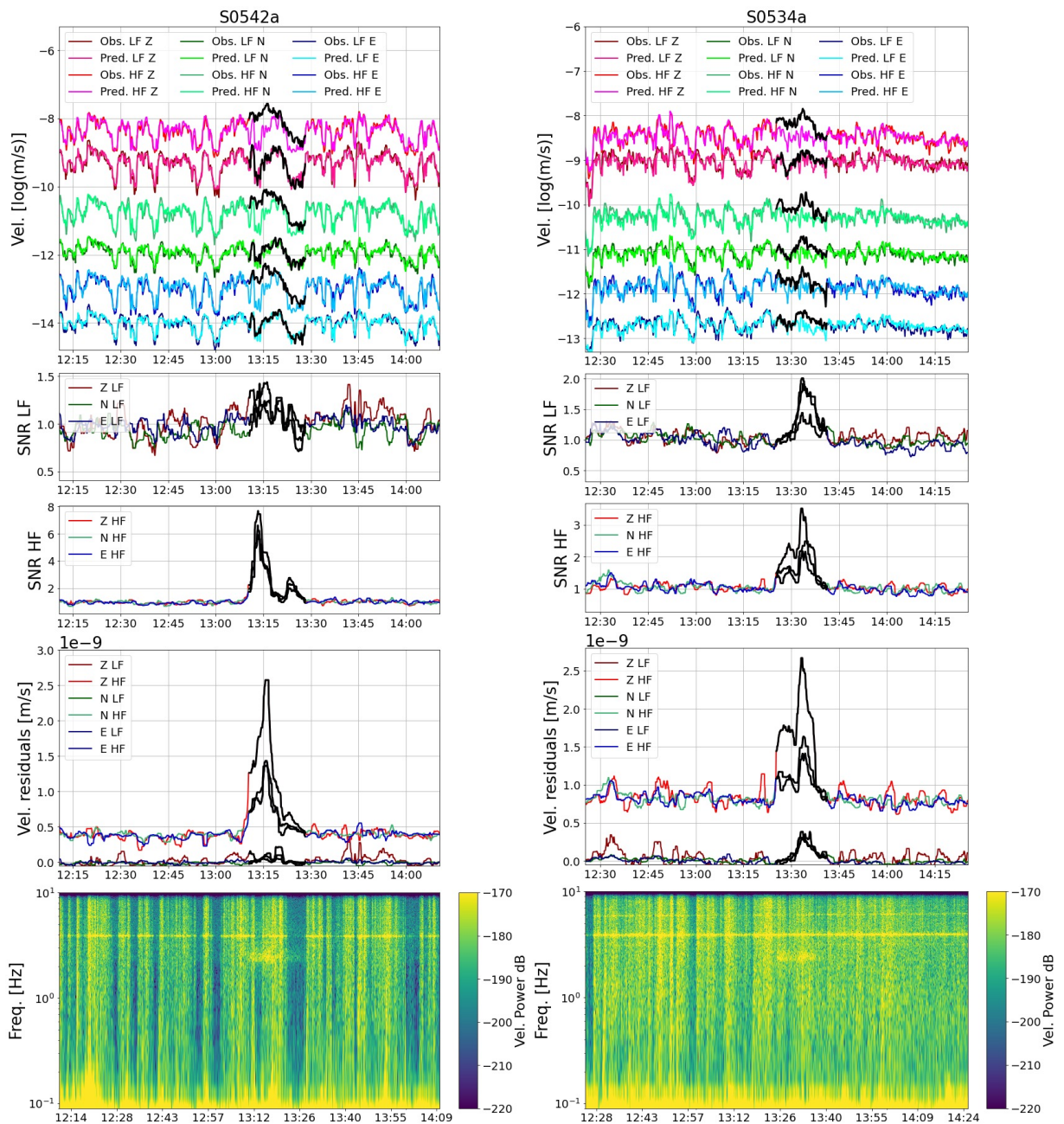


Figure 12. The NN model predictions and SNR analysis for the S0542a VF quality C and S0534a 2.4Hz quality C events.

and the LF SNR for both events is around 3. The S0325a event takes place in a fairly noise period, however, two phase arrivals are apparent in the observed low frequency energy. This is highlighted well in the LF SNR and gives the event its quality B rating meaning its distance can be determined. On the other hand, the S0395a event takes place in a fairly quiet period. To that end, the machine learning predictions are not required to isolate the seismic energy but it does provide a useful framework in which to analyse the event. As it is a BB event there is some energy in the high frequency. It can be

seen that there are two distinct peaks in the high frequency but only one in the low frequency. As it is a C quality only one phase pick is given in the catalogue. Furthermore, the low frequency SNR highlights some energy at low frequencies not indicated in the catalogue. This can also be seen in the spectrogram. This energy emerges from the lower frequencies, similar to atmospheric noise, however, the machine learning has indicated it is separable.

Figure 12 shows two high frequency type events, S0542a and S0534a. These events occur in an extremely noisy period as the season progressed into winter. After S0542a, only 2 events were identified until sol 653. S0542a is a VF quality C event and in spite of the noise, the prediction is able to establish the signal clearly with an SNR of nearly 8. It can be seen that during the event a gust cause this SNR to drop and then recover, in this way we can use the model to assess where the energy of the event is suitable to use and where it may be contaminated by noise. The S0534a event is a 2.4Hz category C event. In the same way as S0542a, the comparison to the model predictions separates the energy of the event from a very noisy background clearly. In opposition to S0542a, the predictions indicate there is some low frequency energy for S0534a with an SNR of up to 2. In both events a slope break can be seen in the residuals of the high frequencies, indicating a possible secondary phase pick. This indicates that the predictions from the machine learning models yields information helpful for the detailed cataloguing of marsquakes.

5.2 Marsquake catalogue analysis

Figure 13 shows the SNR for each event (with available data) throughout the first thousand sols. This does exclude most events later in the mission as power constraints prevented the wind and pressure sensor to be on at all times. The red and blue dots represent the SNR for the HF and LF bandwidths respectively. Notice that several events in the HF group (HF, VF and 2.4 Hz events) have significant low frequency SNRs. This indicates the presence of separable low frequency energy within these events, in contrast to their taxonomy outlined above. This demonstrates that the above observation of low frequency energy in S0534a (in Figure 12) is not unique to that event and is a consistent feature which occurs regularly for all types of high frequency event. The SNR generally modulates with the overall noise level throughout the mission Clinton et al. (2021) in accordance with the level of turbulence in Spiga et al. (2021); Chatain et al. (2021).

Figure 14 shows the high and low frequency SNR versus the distance and magnitudes of the quake from the MQS catalogue for each type of event. There is no clear dependence on distance for the presence of low frequency energy and so the observation is not because these events are close enough to observe this energy. On the other hand, there is a correlation with the magnitude of the event for all high frequency event types. This shows the presence of low frequency energy tends to

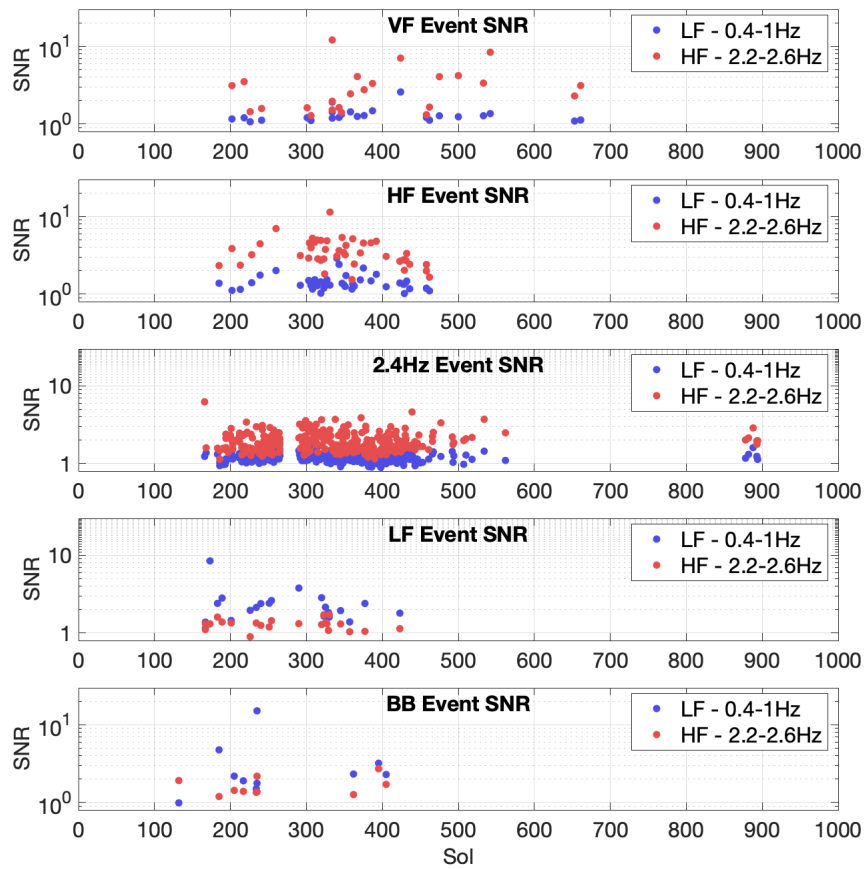


Figure 13. The SNR for the observed seismic energy to the predicted noise levels calculated for the LF 0.4-1Hz and HF 2.2-2.6Hz bandwidths. This is shown for each event class over the mission.

occur more for larger magnitude events, it is not an observational bias. As a result, this suggests that both the high and low frequency event classes are not disparate groupings and that they instead follow a continuum in frequency content.

5.3 Quake detection

New marsquakes can also be directly detected through identifying where the predicted noise level diverges from the observed signal. To do so we must calculate a threshold the residual energy must reach to suggest a seismic event. We propose the following algorithm to calculate a variable threshold as:

- (i) calculate anti-log of the data and subtract the prediction from the observation to obtain a residual

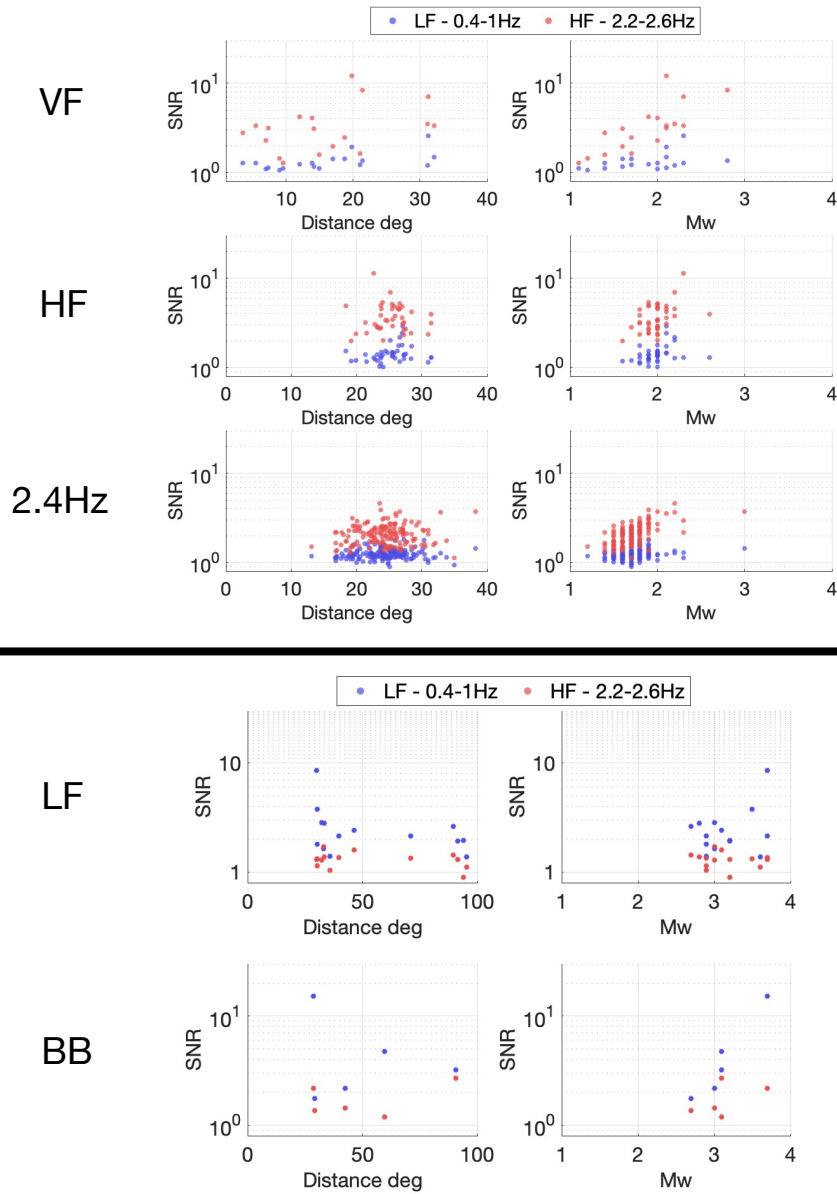


Figure 14. The SNR for the observed seismic energy to the predicted noise levels calculated for the LF 0.4-1Hz and HF 2.2-2.6Hz bandwidths plotted against the marsquake distance and magnitude.

- (ii) filter the residual with a moving median over 100s and subtract the same signal filtered with a moving median over 2000s
- (iii) take the absolute value of the signal and calculate the moving median over 300s
- (iv) calculate the threshold of the mean plus three standard deviations of this signal over a period of 2 hours and advance the window 0.5 hours over the sol.
- (v) detect outliers where the absolute error is above this threshold
- (vi) select outliers only on all three components

(vii) select periods where the detection has positive amplitude as a marsquake will have additional signal

Calculating the threshold in this way is attempting to find an anomalous, outlying, sample within the distribution over the two hours searched.

The detection algorithm performed on the LF, 0.4-1Hz, band found 25 of 32 low frequency and broadband quakes (available with all atmospheric data) in the MQS catalogue (InSight Marsquake Service 2022). Of those not detected, one is the S0405c event which occurs at the very start of the noisy period and has several major glitches nearby. As a result, the residual is very noisy and so difficult to detect the quake as an outlier even though it is observed with an SNR of 2 to the predicted noise level. Another event not detected is S0132a which is quality D and other techniques (Charalambous et al. 2021) have also shown it to be heavily contaminated. The remaining events not detected all have SNR below 1.3 for all components and are all class D or C events. On inspection the energy in these events is mainly below 0.4 Hz so not appropriately represented by the chosen envelope.

of the additional LF detections not part of the MQS catalogue, 34 can be attributed to the high frequency groups of marsquakes. As demonstrated above, this group does often contain low frequency energy. Following this, there are 693 remaining new LF detections. These were further filtered to find more likely marsquake candidates by requiring a minimum detection duration of 2 minutes and an SNR greater than 1.2, leaving 121 new LF detections which were manually reviewed. From this group, we propose 9 new marsquakes which are presented in Table 4. A further 8 possible detections are listed in Table A2 which are not straightforward to confirm but are of interest for catalogue completeness.

The detection algorithm was also ran on the 2.2–2.6 Hz HF envelope. This found 314 out of 377 of the HF event types in the current MQS catalogue (InSight Marsquake Service 2022). Most undetected events are quality D with some C and only 3 quality B events missed. A further 7 of the new detections are associated with the LF grouping of events. The remaining new HF detections were filtered in the same way as for the LF detections above, requiring a minimum duration of 2 minutes and an SNR greater than 1.2. This yields 215 new detection candidates to examine. The manual review of these detections gives an extra 25 new marsquakes presented in Table 5 and a further 26 possible detections in Table A3. Of these new HF detections 2 are shared with the new LF detections.

Figure 15 shows two new LF events detected on Sol 452 and 248. The sol 452 event is an example of a detection in a noisy period, however, it is clearly separate from the environment and also exceeds the confidence interval of the local GP model, shown in Figure 16. The sol 248 event is an example of a low amplitude event in a quiet period. Figure 17 shows two new HF events detected on sol 313 and 502. The sol 502 event is in a very noisy period but there is clear divergent HF and some LF energy. The sol 313 event is during a relatively quiet period. During these quiet periods, the variation of the seismic

Event sol	UTC time	Type	SNRZ LF
190	2019-06-10T07:44:46	LF	1.48
205	2019-06-25T18:45:03	BB	1.35
214	2019-07-04T23:43:09	BB	1.46
248	2019-08-08T20:32:23	LF	1.77
336	2019-11-07T09:54:51	BB/HF	1.23
345	2019-11-16T16:31:35	LF	1.65
395	2020-01-06T20:46:37	LF	1.39
434	2020-02-15T21:41:58	BB/HF	1.46
452	2020-03-05T07:11:54	LF	1.66

Table 4. new LF type events

energy around 2.4Hz is due to the ambient variation of the 2.4Hz resonance, the generation of which has yet to be determined. As noted above, the machine learning models do not predict this ambient variation and usually outputs a constant level as demonstrated in the sol 313 event. Some detections can be due to an increase in this ambient variation making. Therefore, there is a threshold point at which such a variation should be termed an event. This machine learning prediction can help isolate when the background variation is due to atmospheric injection or the ambient 2.4Hz and therefore aid this classification. The isolation of the ambient variation of the 2.4Hz mode may also help identify its generative source. These events are typical of many of the new detections, either in noisy changeable conditions or very low amplitude events, both difficult to detect by eye and so difficult to be caught by the MQS. This highlights how the machine learning predictions can be used to aid marsquake detection and provide new information to add confidence to a difficult detection.

The false detections occur due to particularities in the data, owing to the fact that the detection algorithm specifically identifies outliers in the data. Several false detections are due to data artifacts such as large glitches/donks or dropout/discontinuity in the atmospheric data. Moreover, some false detections occur during long periods with a consistent noise level. Another source of false detections is due to erroneous predictions during the daytime, high noise period, which generally has the highest amplitude and fastest varying signal.

5.4 Seismic detectivity

The threshold obtained in the detection algorithm effectively dictates the energy level required of a marsquake to be detected at that point in time. Tracking this threshold over the mission enables an estimate the detectability of a marsquake similar to one in the catalogue over the mission. Note, how-

Event sol	UTC time	Type	SNRZ HF
166	2019-05-16T14:36:57	2.4Hz	1.35
250	2019-08-10T03:34:41	2.4Hz	1.96
254	2019-08-15T04:08:50	2.4Hz	1.65
291	2019-09-21T10:59:04	2.4Hz	1.73
303	2019-10-04T10:27:15	2.4Hz	1.40
313	2019-10-14T13:43:23	2.4Hz	1.48
313	2019-10-14T18:09:01	2.4Hz	1.62
314	2019-10-15T18:38:26	2.4Hz	1.75
317	2019-10-18T16:53:42	2.4Hz	1.61
326	2019-10-27T22:15:32	2.4Hz	1.49
331	2019-11-02T05:04:35	2.4Hz	1.53
333	2019-11-04T08:23:55	2.4Hz	1.76
336	2019-11-07T09:51:19	HF/BB	1.57
338	2019-11-08T17:37:39	HF/BB	1.48
338	2019-11-09T07:52:22	2.4Hz	1.69
349	2019-11-20T13:29:37	2.4Hz	1.48
351	2019-11-22T16:59:05	2.4Hz	1.33
402	2020-01-14T05:33:52	HF/VF	1.46
431	2020-02-12T19:40:40	2.4Hz	1.27
434	2020-02-15T21:43:03	BB/HF	1.44
446	2020-02-28T05:36:02	2.4Hz	1.65
464	2020-03-17T20:39:36	2.4Hz	1.39
466	2020-03-19T19:37:39	2.4Hz	1.48
502	2020-04-25T13:29:34	BB/VF	2.52
589	2020-07-23T15:04:43	2.4Hz/HF	1.63

Table 5. new HF type events

ever, that the detection level is not a true noise level, it is the level for the residual signal smoothed and detrended as in the detection algorithm. As a result, we can only empirically interpret the detectability in relation to the events observed rather than state the true noise level.

Figure 18 shows, for both the LF (0.4–1 Hz) and HF (2.2–2.6 Hz) bandwidths, the histogram (in orange) of the signal level each marsquake reached to break the threshold is also shown in Figure 18. Notice that the event level histograms are positively skewed, indicating that smaller marsquakes are likely hidden below the noise level. This can be compared to the cumulative distribution of the detection threshold obtained over the mission predictions, shown as the blue curve. This cumulative

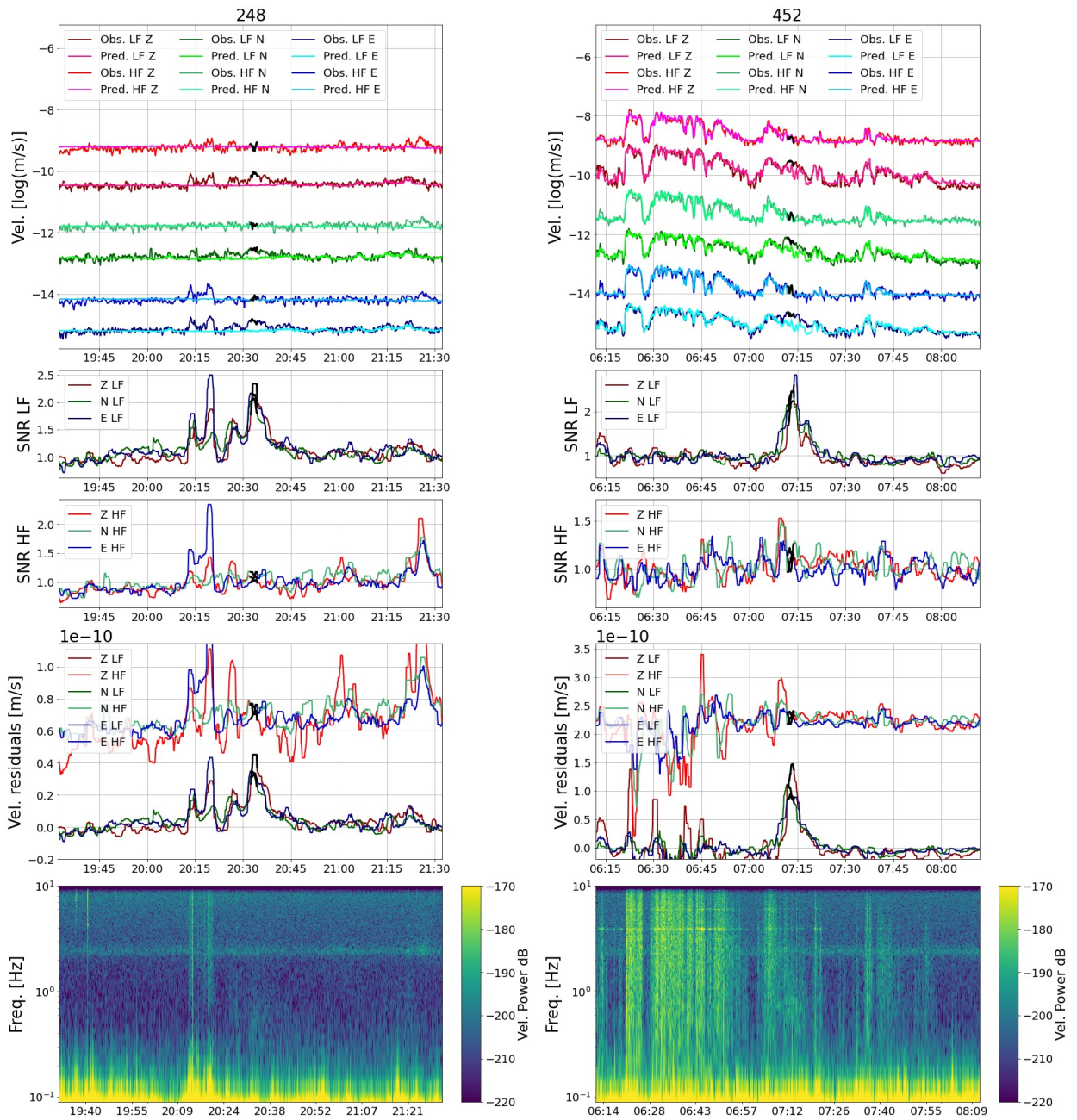


Figure 15. Newly detected LF events

distribution indicates the percentage of time in the dataset for which the detection threshold is at or below such a level. As a result, the comparison between this distribution and detection level histogram then yields the amount of the time where a similar event could be observed. For example, the largest LF and HF type events reached a level of $\sim 1e - 9$ m/s for which the probability of the detection threshold being below is ~ 1 and so they could be seen almost the entire time. This means that events similar to the largest in the data have likely to not have been missed. The median event occurs at

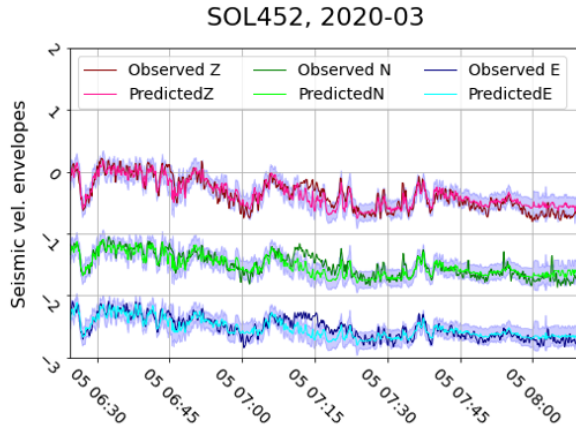


Figure 16. The new LF event detected with the local GP model.

$1e - 10.6$ m/s for LF and $1e - 10.2$ m/s for HF, for which the noise level is at or below for $\sim 45\%$ and $\sim 50\%$ of the time respectively. Finally, the smallest events are at $1e - 10.9$ m/s for the LF and $1e - 11.0$ m/s for HF for which the noise levels are at or below for $\sim 20\%$ and $\sim 5\%$ of the time respectively.

6 CONCLUSION

This work implemented gaussian process regression and a neural network to predict the seismic energy, as seen by SEIS on InSight, generated from the wind and other atmospheric data. This was done for a low frequency (0.4-1Hz) and high frequency (2.2-2.6Hz) bandwidth in order to examine the two main frequency bands marsquakes are observed. We showed how the relationship between seismic energy and each input atmospheric variable varies across the Martian sol and seasons, owing to the different forcing from different turbulent conditions. We implement machine learning as a regression style problem for this task, using mathematical complexity to account for a myriad of such factors.

The neural network was found to have the best performance for both LF and HF regions across the entire dataset in terms of RMSE. As such it is the most useful for marsquake analysis. However, the GPs confidence interval is useful to understand the uncertainty around a prediction and may be of more interest for future work to unpick the impact of the different atmospheric data variables and inform physical models.

The neural network model's prediction was used to first analyse the energy envelope of several marsquakes and derive an SNR (in terms of energy) across the marsquake catalogue. This demonstrated how it can be used for specific event analysis. Examining the SNR for both LF and HF predictions found that the high frequency group (HF, VF and 2.4Hz events) consistently contain low

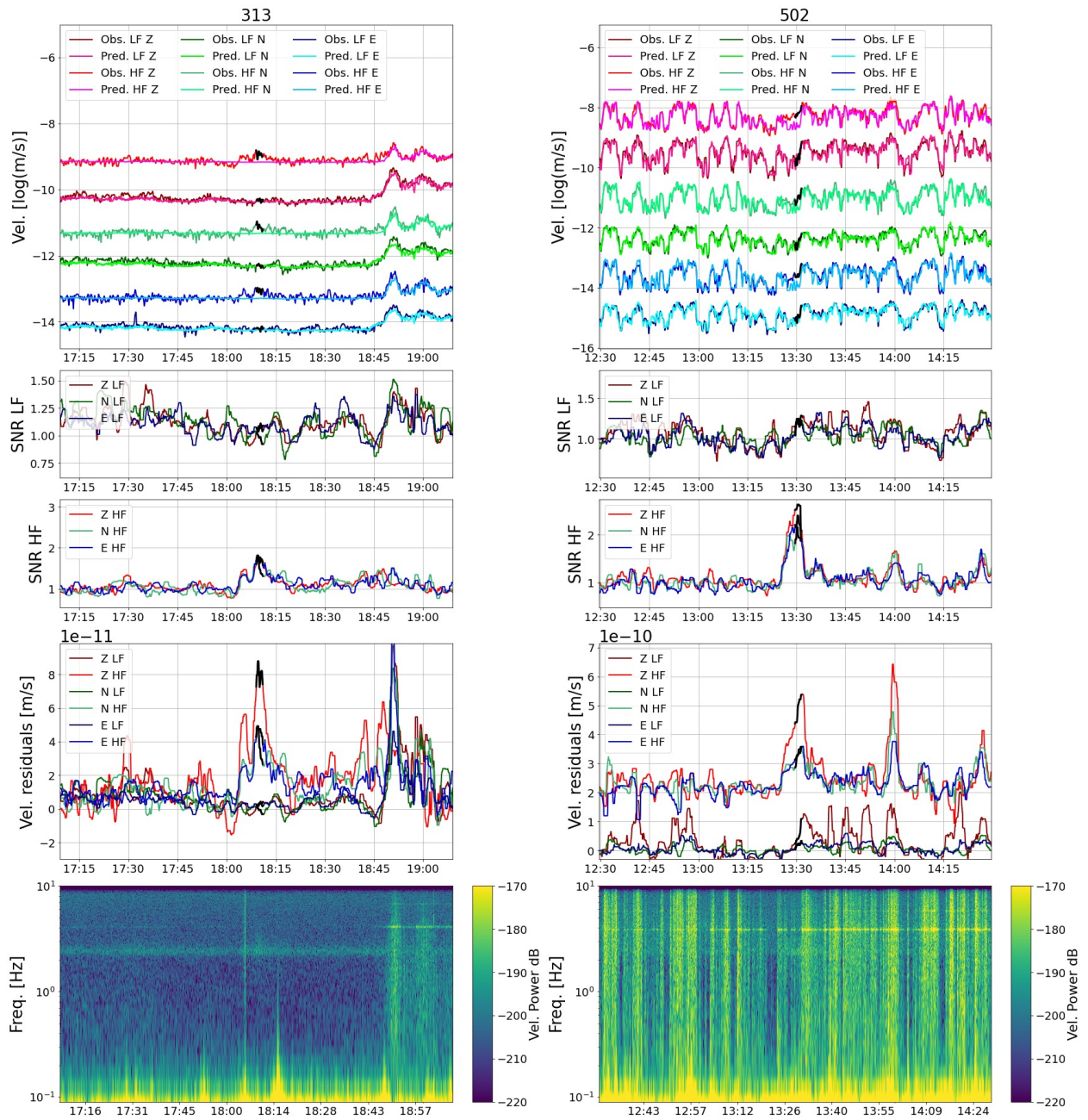


Figure 17. Newly detected HF events

frequency energy with increasing event magnitude. This demonstrates that the marsquake events family is more of a continuum, rather than disparate groupings.

An algorithm was proposed to automatically detect marsquakes. This has led to the detection of 32 new marsquakes and a further 34 possible candidates. The detection algorithm is based on identifying a poor prediction of the observed seismic energy as an outlying event through a variable threshold for the residual of the prediction. This threshold yields an empirical way to determine the detectivity of

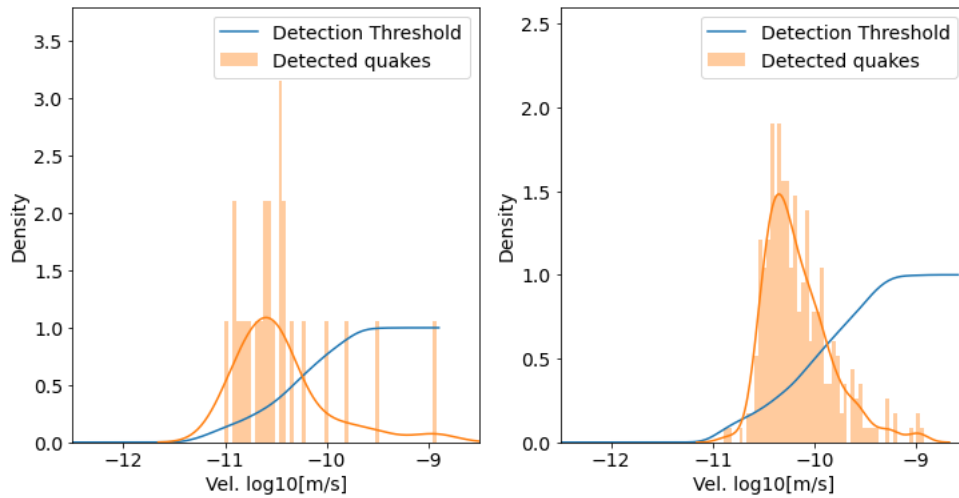


Figure 18. The distribution of detection threshold and events. The blue curve is the cumulative distribution of the detection algorithm threshold and the orange is the histogram/KDE of the level at which the low frequency (left) and high frequency (right) groups of events were detected as being outliers.

marsquakes of a certain size. The cumulative distribution of the threshold gives the amount of time in the mission where the noise level is at or below this level. Comparing this threshold to the catalogue of marsquakes showed that it is unlikely any marsquakes similar to the largest observed have been missed, whereas the median marsquake could be observed $\sim 45\%$ and $\sim 50\%$ of the time for LF and HF events respectively. Through aiding catalogue completeness and analysing marsquake detectivity, this work can be used to help place constraints on the seismicity of Mars.

The detection algorithm could be developed for implementation on board missions to optimise data downlink, such as that proposed by Civilini et al. (2021). Our proposed algorithm can rank the detection in terms of SNR and so the threshold at which a detection would be downlinked is flexible depending on downlink resources. Other future advances could consider the use of a machine learning model in conjunction with a physical model. In this way, it could utilise the InSight data as prior information to help predict noise levels for future missions as in Mimoun et al. (2017).

This work highlights the use of machine learning for consistent treatment of large-scale data in planetary missions. Owing to this consistent treatment, information can be deduced and catalogued repeatably. This represents a sensible approach for (extremely valuable) planetary data and can be considered in geophysical data on the Earth.

DATA AVAILABILITY

SEIS data are referenced at http://dx.doi.org/10.18715/SEIS.INSIGHT.XB_2016. The Mars Quake service (MQS) catalogue of events used in this contribution is the Mars Seismic Catalogue, InSight

Mission, V9 acknowledging ETHZ, IPGP, JPL, ICL, ISAE-Supaero, MPS, and the University of Bristol. It is available at <http://doi.org/10.12686/a14>.

ACKNOWLEDGMENTS

This paper is InSight contribution number 264. We acknowledge NASA, CNES, their partner agencies and institutions (UKSA, SSO, DLR, JPL, IPGP-CNRS, ETHZ, IC, MPS-MPG) and the flight operations team at JPL, SISMOC, MSDS, IRIS-DMC and PDS for providing SEED SEIS data. This work was supported by funding from the French Space Agency CNES and ANR (ANR-19-CE31-0008-08). We also acknowledge the help of the CALMIP computing cluster.

REFERENCES

- Banfield, D., Rodriguez-Manfredi, J., Russell, C., Rowe, K., Leneman, D., Lai, H., Cruce, P., Means, J., Johnson, C., Mittelholz, A., et al., 2019. Insight auxiliary payload sensor suite (apss), *Space Science Reviews*, **215**(1), 1–33.
- Banfield, D., Spiga, A., Newman, C., Forget, F., Lemmon, M., Lorenz, R., Murdoch, N., Viudez-Moreiras, D., Pla-Garcia, J., Garcia, R. F., et al., 2020. The atmosphere of mars as observed by insight, *Nature Geoscience*, **13**(3), 190–198.
- Barkaoui, S., Lognonné, P., Kawamura, T., Stutzmann, É., Seydoux, L., de Hoop, M. V., Balestrieri, R., Scholz, J.-R., Sainton, G., Plasman, M., et al., 2021. Anatomy of continuous mars seis and pressure data from unsupervised learning, *Bulletin of the Seismological Society of America*, **111**(6), 2964–2981.
- Beyreuther, M., Barsch, R., Krischer, L., Megies, T., Behr, Y., & Wassermann, J., 2010. Obspy: A python toolbox for seismology, *Seismological Research Letters*, **81**(3), 530–533.
- Ceylan, S., Clinton, J. F., Giardini, D., Böse, M., Charalambous, C., van Driel, M., Horleston, A., Kawamura, T., Khan, A., Orhand-Mainsant, G., et al., 2021. Companion guide to the marsquake catalog from insight, sols 0–478: Data content and non-seismic events, *Physics of the Earth and Planetary Interiors*, **310**, 106597.
- Charalambous, C., Stott, A. E., Pike, T., McClean, J. B., Warren, T., Spiga, A., Banfield, D., Garcia, R. F., Clinton, J. F., Stähler, S. C., et al., 2021. A comodulation analysis of atmospheric energy injection into the ground motion at insight, mars, *Journal of Geophysical Research. Planets*.
- Chatain, A., Spiga, A., Banfield, D., Forget, F., & Murdoch, N., 2021. Seasonal variability of the daytime and nighttime atmospheric turbulence experienced by insight on mars, *Geophysical Research Letters*, **48**(22), e2021GL095453.
- Chollet, F. et al., 2015. Keras, <https://keras.io>.
- Civilini, F., Weber, R., Jiang, Z., Phillips, D., & Pan, W. D., 2021. Detecting moonquakes using convolutional neural networks, a non-local training set, and transfer learning, *Geophysical Journal International*, **225**(3), 2120–2134.

- Clinton, J. F., Ceylan, S., van Driel, M., Giardini, D., Stähler, S. C., Böse, M., Charalambous, C., Dahmen, N. L., Horleston, A., Kawamura, T., et al., 2021. The marsquake catalogue from insight, sols 0–478, *Physics of the Earth and Planetary Interiors*, **310**, 106595.
- Compaire, N., Margerin, L., Garcia, R. F., Pinot, B., Calvet, M., Orhand-Mainsant, G., Kim, D., Lekic, V., Tauzin, B., Schimmel, M., et al., 2021. Autocorrelation of the ground vibrations recorded by the seis-insight seismometer on mars, *Journal of Geophysical Research: Planets*, **126**(4), e2020JE006498.
- Cybenko, G., 1989. Approximation by superpositions of a sigmoidal function, *Mathematics of control, signals and systems*, **2**(4), 303–314.
- Dahmen, N. L., Clinton, J. F., Ceylan, S., van Driel, M., Giardini, D., Khan, A., Stähler, S. C., Böse, M., Charalambous, C., Horleston, A., et al., 2021a. Super high frequency events: A new class of events recorded by the insight seismometers on mars, *Journal of Geophysical Research: Planets*, **126**(2), e2020JE006599.
- Dahmen, N. L., Zenhäusern, G., Clinton, J. F., Giardini, D., Stähler, S. C., Ceylan, S., Charalambous, C., van Driel, M., Hurst, K. J., Kedar, S., et al., 2021b. Resonances and lander modes observed by insight on mars (1–9 hz), *Bulletin of the Seismological Society of America*, **111**(6), 2924–2950.
- Garcia, R. F., Kenda, B., Kawamura, T., Spiga, A., Murdoch, N., Lognonné, P. H., Widmer-Schmidrig, R., Compaire, N., Orhand-Mainsant, G., Banfield, D., et al., 2020. Pressure effects on the seis-insight instrument, improvement of seismic records, and characterization of long period atmospheric waves from ground displacements, *Journal of Geophysical Research: Planets*, **125**(7), e2019JE006278.
- Giardini, D., Lognonné, P., Banerdt, W. B., Pike, W. T., Christensen, U., Ceylan, S., Clinton, J. F., van Driel, M., Stähler, S. C., Böse, M., et al., 2020. The seismicity of mars, *Nature Geoscience*, **13**(3), 205–212.
- Goodfellow, I., Bengio, Y., & Courville, A., 2016. *Deep learning*, MIT press.
- GPy, since 2012. GPy: A gaussian process framework in python, <http://github.com/SheffieldML/GPy>.
- Hobiger, M., Hallo, M., Schmelzbach, C., Stähler, S., Fäh, D., Giardini, D., Golombek, M., Clinton, J., Dahmen, N., Zenhäusern, G., et al., 2021. The shallow structure of mars at the insight landing site from inversion of ambient vibrations, *Nature communications*, **12**(1), 1–13.
- Hurst, K., Fayon, L., Knapmeyer-Endrun, B., Schmelzbach, C., van Driel, M., Ervin, J., Kedar, S., Pike, W. T., Calcutt, S., Warren, T., et al., 2021. Resonances of the insight seismometer on mars, *Bulletin of the Seismological Society of America*, **111**(6), 2951–2963.
- InSight Marsquake Service, 2022. Mars Seismic Catalogue, InSight Mission; V9 2022-01-01, ETHZ, IPGP, JPL, ICL, ISAE-Supaero, MPS, Univ. Bristol. doi: 10.12686/a14.
- Johnson, C. W., Ben-Zion, Y., Meng, H., & Vernon, F., 2020. Identifying different classes of seismic noise signals using unsupervised learning, *Geophysical Research Letters*, **47**(15), e2020GL088353.
- Kenda, B., Drilleau, M., Garcia, R. F., Kawamura, T., Murdoch, N., Compaire, N., Lognonné, P., Spiga, A., Widmer-Schmidrig, R., Delage, P., et al., 2020. Subsurface structure at the insight landing site from compliance measurements by seismic and meteorological experiments, *Journal of Geophysical Research: Planets*, **125**(6), e2020JE006387.
- Khan, A., Ceylan, S., van Driel, M., Giardini, D., Lognonné, P., Samuel, H., Schmerr, N. C., Stähler, S. C.,

- Duran, A. C., Huang, Q., et al., 2021. Upper mantle structure of mars from insight seismic data, *Science*, **373**(6553), 434–438.
- Kingma, D. P. & Ba, J., 2014. Adam: A method for stochastic optimization, *arXiv preprint arXiv:1412.6980*.
- Knapmeyer-Endrun, B. & Hammer, C., 2015. Identification of new events in apollo 16 lunar seismic data by hidden markov model-based event detection and classification, *Journal of Geophysical Research: Planets*, **120**(10), 1620–1645.
- Knapmeyer-Endrun, B., Panning, M. P., Bissig, F., Joshi, R., Khan, A., Kim, D., Lekić, V., Tauzin, B., Thari-mena, S., Plasman, M., et al., 2021. Thickness and structure of the martian crust from insight seismic data, *Science*, **373**(6553), 438–443.
- Krischer, L., Megies, T., Barsch, R., Beyreuther, M., Lecocq, T., Caudron, C., & Wassermann, J., 2015. Obspy: A bridge for seismology into the scientific python ecosystem, *Computational Science & Discovery*, **8**(1), 014003.
- Lognonné, P., Banerdt, W. B., Giardini, D., Pike, W., Christensen, U., Laudet, P., De Raucourt, S., Zweifel, P., Calcutt, S., Bierwirth, M., et al., 2019. Seis: Insight’s seismic experiment for internal structure of mars, *Space Science Reviews*, **215**(1).
- Lognonné, P., Banerdt, W., Pike, W., Giardini, D., Christensen, U., Garcia, R. F., Kawamura, T., Kedar, S., Knapmeyer-Endrun, B., Margerin, L., et al., 2020. Constraints on the shallow elastic and anelastic structure of mars from insight seismic data, *Nature Geoscience*, **13**(3), 213–220.
- Megies, T., Beyreuther, M., Barsch, R., Krischer, L., & Wassermann, J., 2011. Obspy—what can it do for data centers and observatories?, *Annals of Geophysics*, **54**(1), 47–58.
- Mimoun, D., Murdoch, N., Lognonné, P., Hurst, K., Pike, W. T., Hurley, J., Nébut, T., & Banerdt, W. B., 2017. The noise model of the seis seismometer of the insight mission to mars, *Space Science Reviews*, **211**(1), 383–428.
- Murdoch, N., Mimoun, D., Garcia, R. F., Rapin, W., Kawamura, T., Lognonné, P., Banfield, D., & Banerdt, W. B., 2017. Evaluating the wind-induced mechanical noise on the insight seismometers, *Space Science Reviews*, **211**(1), 429–455.
- Murdoch, N., Alazard, D., Knapmeyer-Endrun, B., Teanby, N., & Myhill, R., 2018. Flexible mode modelling of the insight lander and consequences for the seis instrument, *Space Science Reviews*, **214**(8), 1–24.
- Murphy, K. P., 2012. *Machine learning: a probabilistic perspective*, MIT press.
- Schimmel, M., Stutzmann, E., Lognonné, P., Compaire, N., Davis, P., Drilleau, M., Garcia, R., Kim, D., Knapmeyer-Endrun, B., Lekic, V., et al., 2021. Seismic noise autocorrelations on mars, *Earth and Space Science*, p. e2021EA001755.
- Scholz, J.-R., Widmer-Schmidrig, R., Davis, P., Lognonné, P., Pinot, B., Garcia, R. F., Hurst, K., Pou, L., Nimmo, F., Barkaoui, S., et al., 2020. Detection, analysis, and removal of glitches from insight’s seismic data from mars, *Earth and Space Science*, **7**(11), e2020EA001317.
- Service, I. M. S. D., 2019. Seis raw data, insight mission.
- Seydoux, L., Balestrieri, R., Poli, P., Hoop, M. d., Campillo, M., & Baraniuk, R., 2020. Clustering earth-

quake signals and background noises in continuous seismic data with unsupervised deep learning, *Nature communications*, **11**(1), 1–12.

Spiga, A., Murdoch, N., Lorenz, R., Forget, F., Newman, C., Rodriguez, S., Pla-Garcia, J., Moreiras, D. V., Banfield, D., Perrin, C., et al., 2021. A study of daytime convective vortices and turbulence in the martian planetary boundary layer based on half-a-year of insight atmospheric measurements and large-eddy simulations, *Journal of Geophysical Research: Planets*, **126**(1), e2020JE006511.

Stähler, S. C., Khan, A., Banerdt, W. B., Lognonné, P., Giardini, D., Ceylan, S., Drilleau, M., Duran, A. C., Garcia, R. F., Huang, Q., et al., 2021. Seismic detection of the martian core, *Science*, **373**(6553), 443–448.

Stott, A. E., Charalambous, C., Warren, T. J., Pike, W. T., Myhill, R., Murdoch, N., McClean, J. B., Trebi-Ollennu, A., Lim, G., Garcia, R. F., et al., 2021. The site tilt and lander transfer function from the short-period seismometer of insight on mars, *Bulletin of the Seismological Society of America*, **111**(6), 2889–2908.

Williams, C. K. & Rasmussen, C. E., 2006. *Gaussian processes for machine learning*, vol. 2, MIT press Cambridge, MA.

Table A1. Data channels

Data type	Channels				
	20 sps	10 sps	1 sps	0.5 sps	0.1 sps
VBB velocity U, V and W	02.BHU	03.BHU			
Wind speed boom 1 and 2			10.LWS	10.VWS	13.VWS
Wind direction boom 1 and 2			10.LWD	10.VWD	13.VWD
Air temperature boom 1 and 2			10.LKO	10.VKO	13.VKO
Pressure	12.BDO	13.BDO	10.LDO		

APPENDIX A: DATA CHANNELS

Table A2. possible LF type events

Event sol	UTC time	SNRZ LF
195	2019-06-10T07:44:46	1.55
255	2019-08-15T22:55:39	1.86
260	2019-08-21T02:59:02	1.34
312	2019-10-13T17:42:24	1.42
356	2019-11-27T21:58:12	1.33
379	2019-12-21T10:38:48	1.30
440	2020-02-22T06:39:53	1.33
466	2020-03-19T17:38:35	1.52

APPENDIX B: LIST OF POSSIBLE NEW DETECTIONS

Table A3. possible HF type events

Event sol	UTC time	SNRZ HF
177	2019-05-27T04:58:12	1.60
193	2019-06-13T09:38:01	1.51
199	2019-06-18T19:19:12	1.70
199	2019-06-18T21:39:59	1.56
204	2019-06-24T02:03:10	1.62
220	2019-07-10T13:59:20	1.34
223	2019-07-14T06:12:03	2.01
258	2019-08-19T03:40:06	1.30
312	2019-10-13T14:02:22	1.35
320	2019-10-21T21:37:39	1.56
320	2019-10-22T00:10:47	1.50
326	2019-10-27T22:53:19	1.40
329	2019-10-31T03:00:28	1.37
332	2019-11-03T03:57:05	1.43
335	2019-11-06T08:10:07	1.39
336	2019-11-07T04:51:20	1.54
350	2019-11-21T15:14:01	1.35
355	2019-11-26T18:57:03	1.37
391	2020-01-02T17:50:11	1.51
429	2020-02-10T20:19:53	1.43
441	2020-02-23T01:40:16	1.47
455	2020-03-08T12:14:17	1.82
457	2020-03-10T12:52:55	1.55
497	2020-04-20T14:39:15	1.74
502	2020-04-25T07:18:54	1.46
680	2020-10-25T18:15:29	1.39

APPENDIX C: SNR TABLE OF CATALOGUED MARSQUAKES

Event Name	SNRZ LF	SNRN LF	SNRE LF	SNRZ HF	SNRN HF	SNRE HF
S0423a	1.80	1.59	1.66	1.14	1.07	1.20
S0405c	2.29	2.05	2.08	1.71	1.43	1.42
S0395a	3.20	2.98	2.65	2.71	2.70	2.21
S0377c	2.40	2.13	2.14	1.05	1.06	1.02
S0362b	2.32	2.61	2.30	1.26	1.10	1.17
S0357a	1.39	1.12	1.24	1.04	1.01	0.97
S0345a	1.94	2.42	1.92	1.31	1.17	1.23
S0330a	1.60	1.44	1.56	1.72	1.42	1.45
S0329b	1.83	2.14	1.76	1.08	0.99	1.09
S0327d	1.60	2.17	1.95	1.31	1.18	1.30
S0325a	2.15	1.79	2.12	1.36	1.39	1.35
S0323d	1.65	2.17	1.66	1.71	1.57	1.56
S0320b	2.85	2.42	2.44	1.28	1.40	1.38
S0290b	3.79	3.84	4.80	1.32	1.26	1.19
S0254b	2.62	2.34	2.34	1.44	1.41	1.23
S0251a	2.42	2.17	2.02	1.20	1.13	1.09
S0240a	2.39	2.28	2.38	1.25	1.20	1.12
S0235c	1.76	1.71	1.73	1.36	1.63	1.84
S0235b	15.17	15.40	14.63	2.18	2.08	2.68
S0234d	1.50	1.64	1.50	1.35	1.27	1.18
S0234c	2.13	1.74	2.24	1.34	1.22	1.29
S0226b	1.96	1.97	1.92	0.90	0.98	1.03
S0217a	1.90	1.47	1.89	1.39	1.30	1.19
S0205a	2.18	2.10	2.32	1.43	1.18	1.13
S0201a	1.45	1.60	1.49	1.35	1.10	1.11
S0189a	2.82	2.40	2.47	1.38	1.29	1.19
S0185a	4.76	3.97	4.31	1.19	1.31	1.08
S0183a	2.41	1.88	2.34	1.60	1.26	1.22
S0173a	8.50	9.80	10.32	1.31	1.20	1.09
S0167b	1.14	1.35	1.16	1.32	1.18	1.17
S0167a	1.38	1.29	1.23	1.11	1.03	1.09
S0132a	0.99	1.21	1.29	1.91	1.39	1.37
S0894a	1.13	1.22	1.12	1.97	1.69	1.51
S0893c	1.24	1.41	1.34	1.77	1.58	1.52
S0893b	1.21	1.66	1.62	1.96	1.72	1.65
S0888b	1.61	1.57	1.63	2.88	2.13	2.27
S0882b	1.31	1.23	1.27	2.14	1.87	1.66
S0878a	1.17	1.21	1.14	2.01	1.71	1.66
S0661a	1.13	1.24	1.21	3.13	1.97	2.24
S0653a	1.09	1.15	1.09	2.29	1.90	1.65
S0562a	1.10	0.95	1.00	2.49	1.99	1.63
S0542a	1.36	1.44	1.38	8.41	5.57	5.29
S0534a	1.44	2.01	1.92	3.72	2.41	1.98
S0533a	1.28	1.23	1.06	3.36	2.27	1.89
S0518a	1.13	1.16	1.13	2.17	1.52	1.55

Event Name	SNRZ LF	SNRN LF	SNRE LF	SNRZ HF	SNRN HF	SNRE HF
S0510a	1.29	1.09	1.08	2.09	1.82	1.79
S0507a	0.98	1.04	0.90	1.98	1.78	1.61
S0500a	1.24	1.26	1.16	4.20	2.97	2.70
S0494a	1.26	1.48	1.22	1.87	1.52	1.36
S0493a	1.04	1.17	1.13	1.76	1.58	1.43
S0492a	1.43	1.21	1.22	2.20	1.70	1.81
S0477a	1.23	1.05	1.00	3.35	3.14	2.88
S0475a	1.27	1.08	1.01	4.07	3.70	2.90
S0467a	1.41	1.35	1.26	2.52	2.00	1.98
S0466b	1.33	1.47	1.54	2.24	1.72	1.96
S0466a	1.36	1.52	1.52	1.93	1.50	1.52
S0462b	1.10	1.12	1.17	1.65	1.37	1.33
S0462a	1.12	1.06	1.18	1.65	1.45	1.21
S0461f	1.14	1.10	1.19	1.51	1.37	1.43
S0458b	1.19	1.21	1.12	2.40	1.90	1.78
S0458a	1.18	1.15	1.18	1.99	1.92	1.74
S0458d	1.21	1.03	1.03	1.31	1.29	1.15
S0453a	1.03	1.08	1.04	1.66	1.59	1.69
S0450a	1.02	1.18	1.04	1.66	1.48	1.44
S0448a	1.06	1.10	1.09	2.33	1.77	1.78
S0446a	1.14	1.10	1.12	1.83	1.45	1.37
S0443b	1.02	1.05	1.02	1.92	1.90	1.68
S0443a	0.94	1.03	1.00	1.51	1.50	1.37
S0440a	1.24	1.20	1.22	1.76	1.58	1.59
S0439a	1.36	1.30	1.38	4.62	3.17	2.86
S0436c	1.17	1.15	1.16	2.42	2.45	2.21
S0436b	1.13	1.17	1.17	1.58	1.71	1.41
S0432a	1.47	1.50	1.70	3.34	2.65	2.45
S0432b	1.45	1.31	1.38	1.76	1.80	1.77
S0431c	1.32	1.36	1.40	2.08	1.74	1.59
S0431b	1.42	1.30	1.52	2.71	2.30	2.11
S0430d	1.40	1.12	1.25	1.69	1.31	1.29
S0430c	1.12	1.13	1.25	2.85	2.57	1.93
S0430b	1.23	1.14	1.20	1.90	1.41	1.53
S0430a	1.23	1.14	1.26	2.33	2.06	1.77
S0429b	1.24	1.32	1.30	1.98	1.83	1.74
S0429a	1.02	1.19	1.14	2.03	1.79	1.76
S0428c	0.94	1.07	1.05	1.55	1.39	1.44
S0428b	1.13	1.02	1.03	1.68	1.42	1.35
S0428a	1.33	1.23	1.31	2.76	2.31	2.08
S0427a	1.14	1.34	1.17	1.94	1.75	1.72
S0424c	2.58	2.44	2.72	7.05	5.91	5.14
S0424b	1.16	1.40	1.13	1.56	1.31	1.30
S0424a	1.10	1.02	1.01	1.41	1.25	1.22
S0423c	1.39	1.28	1.33	2.65	2.41	2.44

Event Name	SNRZ LF	SNRN LF	SNRE LF	SNRZ HF	SNRN HF	SNRE HF
S0423b	1.23	1.06	1.16	1.94	1.85	1.93
S0422a	1.17	1.02	0.93	1.47	1.47	1.40
S0420b	1.19	1.19	1.17	1.76	1.54	1.48
S0419a	1.00	1.24	1.16	2.07	1.65	1.78
S0418a	1.20	1.20	1.22	2.61	2.21	2.18
S0417b	1.17	1.14	1.08	1.38	1.50	1.42
S0417a	1.25	1.23	1.33	2.32	2.06	1.90
S0415a	1.10	1.07	1.01	2.38	1.72	1.54
S0414a	1.24	1.19	1.23	1.50	1.31	1.33
S0413a	1.21	1.02	0.92	1.60	1.34	1.34
S0411c	1.05	1.10	1.09	1.57	1.34	1.28
S0411b	1.18	1.32	1.13	1.74	1.48	1.43
S0411a	1.29	1.25	1.21	2.99	2.74	2.45
S0409c	1.16	1.17	1.18	2.29	1.84	2.14
S0409b	1.23	1.17	1.15	1.45	1.39	1.26
S0409a	1.19	1.24	1.38	1.97	1.77	1.57
S0408b	1.12	1.22	1.28	2.52	2.56	2.14
S0408a	1.34	1.35	1.31	2.43	2.23	1.89
S0405f	1.24	1.37	1.25	3.06	2.58	2.22
S0405e	1.02	1.11	1.06	1.30	1.19	1.15
S0405d	0.99	1.06	1.13	1.44	1.31	1.29
S0405b	1.17	1.06	1.09	2.27	1.82	1.82
S0405a	1.13	1.20	1.15	1.66	1.34	1.49
S0403a	1.12	1.12	0.97	1.41	1.25	1.09
S0401b	1.41	1.68	1.42	2.10	1.65	1.59
S0401a	1.04	1.20	1.07	1.35	1.38	1.34
S0400a	1.59	1.40	1.23	1.87	1.91	1.76
S0398b	1.10	1.16	1.19	1.51	1.59	1.41
S0398a	0.89	1.16	1.08	1.31	1.13	1.15
S0397b	1.15	1.17	1.18	1.97	1.87	1.84
S0397a	1.16	1.41	1.36	2.23	1.90	2.06
S0396a	1.13	1.26	1.30	2.60	2.07	2.12
S0395b	0.98	1.01	1.08	1.44	1.18	1.25
S0394a	1.32	1.23	1.29	2.19	1.86	1.88
S0392a	1.80	1.48	1.75	4.80	3.84	3.33
S0390a	1.28	1.12	1.17	1.15	1.09	1.20
S0388b	0.97	1.30	1.09	1.35	1.35	1.25
S0388a	1.23	1.24	1.16	1.63	1.43	1.49
S0387a	1.48	1.63	1.56	3.33	3.47	2.79
S0386b	0.90	0.95	0.93	1.99	1.94	1.73
S0386a	1.59	1.23	1.18	1.81	1.33	1.36
S0385b	1.14	1.14	1.05	1.74	1.69	1.62
S0385a	1.48	1.42	1.33	4.57	3.56	3.66
S0383c	1.18	1.25	1.32	1.71	1.50	1.51

Event Name	SNRZ LF	SNRN LF	SNRE LF	SNRZ HF	SNRN HF	SNRE HF
S0383b	1.11	1.14	1.11	1.40	1.34	1.24
S0383a	1.10	1.16	1.11	1.72	1.52	1.58
S0382a	0.91	1.05	0.99	1.29	1.22	1.12
S0381f	1.16	1.17	1.20	1.43	1.23	1.21
S0381e	1.23	1.12	1.10	1.59	1.47	1.48
S0381d	1.34	1.27	1.33	1.74	1.76	1.62
S0381c	0.97	1.12	1.00	1.49	1.25	1.33
S0381b	1.25	1.31	1.23	1.21	1.24	1.26
S0381a	1.35	1.24	1.27	1.82	1.56	1.46
S0380a	1.17	1.18	1.22	2.03	1.77	1.77
S0379b	1.07	1.06	1.28	1.62	1.49	1.53
S0379a	1.19	1.10	1.14	1.82	1.53	1.45
S0378b	1.61	1.52	1.66	3.03	2.79	2.52
S0378a	1.26	1.23	1.30	2.68	2.19	1.83
S0377b	1.17	1.20	1.25	1.31	1.30	1.28
S0377a	1.08	1.13	1.11	1.33	1.16	1.13
S0376b	1.17	1.28	1.27	1.67	1.45	1.44
S0376a	1.28	1.32	1.17	2.76	1.92	2.08
S0375a	2.17	2.16	2.45	4.56	3.92	3.08
S0373b	1.28	1.40	1.33	2.50	1.96	1.90
S0373a	1.01	1.10	1.11	1.55	1.54	1.57
S0372a	1.44	1.42	1.42	3.89	3.20	2.69
S0371b	1.52	1.52	1.78	3.39	2.54	2.70
S0371a	1.39	1.26	1.25	1.53	1.36	1.48
S0367d	1.12	1.09	1.08	1.44	1.27	1.30
S0367c	1.11	1.17	1.08	1.97	1.91	1.71
S0367b	1.07	1.14	1.06	1.73	1.39	1.46
S0367a	1.25	1.19	1.15	4.09	3.45	2.75
S0365b	1.16	1.16	1.19	1.54	1.31	1.36
S0365a	1.24	1.15	1.21	1.89	1.75	1.84
S0365c	1.25	1.23	1.24	1.87	1.59	1.50
S0364a	1.19	1.07	1.10	2.18	1.90	1.78
S0363d	1.27	1.22	1.23	2.44	2.17	2.14
S0363c	1.29	1.12	1.20	2.00	1.60	1.67
S0363b	1.19	1.13	1.13	1.67	1.55	1.68
S0363a	1.25	1.14	1.11	2.49	2.07	2.05
S0362c	1.13	1.11	1.14	1.38	1.33	1.33
S0362a	1.06	1.39	1.32	1.42	1.47	1.35
S0361c	1.35	1.28	1.37	5.17	4.03	3.33
S0361b	1.29	1.23	1.26	1.79	1.67	1.68
S0360b	1.16	1.07	1.05	1.54	1.78	1.51
S0360a	1.10	1.01	1.07	1.61	1.66	1.54
S0359a	1.13	1.29	1.09	1.83	1.59	1.67
S0358c	1.43	1.25	1.19	2.44	1.87	1.89
S0358b	1.09	1.05	1.05	1.54	1.48	1.33
S0358a	1.12	1.14	1.14	1.60	1.44	1.43
S0357b	1.37	1.33	1.32	1.64	1.54	1.40
S0355a	1.18	1.16	1.13	3.15	2.65	2.56

Event Name	SNRZ LF	SNRN LF	SNRE LF	SNRZ HF	SNRN HF	SNRE HF
S0354a	1.24	1.15	1.16	1.63	1.49	1.40
S0353d	1.18	1.22	1.14	1.37	1.17	1.25
S0353c	1.22	1.19	1.27	1.49	1.47	1.50
S0353b	1.36	1.41	1.34	2.26	2.17	2.03
S0353a	1.11	1.02	1.03	1.48	1.33	1.24
S0353f	1.43	1.62	1.60	2.34	1.61	1.57
S0353e	1.25	1.13	1.19	2.55	1.94	1.77
S0352b	1.31	1.24	1.25	1.72	1.61	1.71
S0352a	1.73	1.58	1.89	4.24	3.57	3.50
S0351b	1.25	1.28	1.19	3.21	3.19	2.70
S0350a	1.20	1.25	1.22	2.58	2.29	2.25
S0349a	1.33	1.31	1.37	3.43	3.17	2.43
S0349b	1.29	1.33	1.23	2.98	1.83	1.78
S0348d	1.01	0.95	1.00	1.91	1.68	1.44
S0348c	1.61	1.44	1.69	2.37	2.21	1.77
S0348b	1.38	1.22	1.51	2.46	2.17	2.04
S0348a	1.81	1.80	1.71	2.14	1.93	1.70
S0347a	1.38	1.32	1.43	5.37	3.73	4.12
S0346d	1.46	1.50	1.25	2.58	2.03	1.99
S0346c	1.25	1.37	1.25	1.66	1.34	1.30
S0346b	1.05	1.12	1.08	1.39	1.29	1.24
S0346a	1.33	1.34	1.13	1.41	1.45	1.37
S0345b	0.91	0.96	0.94	1.65	1.57	1.49
S0345d	1.09	1.18	1.15	1.31	1.35	1.13
S0345c	1.12	1.08	1.09	1.49	1.32	1.25
S0344b	1.18	1.21	1.20	1.38	1.43	1.39
S0344a	1.20	1.13	1.11	1.64	1.46	1.44
S0343b	2.41	1.87	2.10	3.63	4.26	3.09
S0343a	1.22	1.23	1.31	1.63	2.53	1.76
S0342a	1.37	1.24	1.35	2.30	1.77	2.13
S0341a	1.19	1.25	1.12	1.40	1.45	1.32
S0340b	1.16	1.10	1.10	1.73	1.37	1.53
S0340a	2.90	2.55	2.97	3.08	2.63	2.56
S0339f	1.22	1.10	1.17	1.39	1.33	1.33
S0339b	1.05	1.03	1.08	1.64	1.63	1.31
S0339a	1.20	1.11	1.16	1.52	1.33	1.36
S0339e	1.11	1.11	1.16	1.32	1.30	1.33
S0339d	1.09	1.11	1.18	1.44	1.30	1.26
S0339c	1.37	1.10	1.60	1.74	1.73	1.69
S0338b	1.23	1.15	1.24	3.71	3.48	2.77
S0337a	1.07	1.11	1.09	1.70	1.59	1.45
S0335b	1.09	1.08	1.12	1.51	1.40	1.41
S0335c	1.17	1.15	1.19	1.57	1.55	1.37
S0335a	1.11	1.10	1.13	1.45	1.45	1.34
S0334c	1.19	1.15	1.31	1.52	1.34	1.54

Event Name	SNRZ LF	SNRN LF	SNRE LF	SNRZ HF	SNRN HF	SNRE HF
S0334b	1.43	1.29	1.22	1.96	1.84	1.69
S0334a	1.91	1.85	2.00	12.10	8.28	7.38
S0333a	1.50	1.43	1.43	1.84	1.78	1.60
S0332a	1.00	1.15	1.11	2.27	1.99	2.00
S0331b	1.22	1.25	1.26	2.73	2.49	2.36
S0331a	1.30	1.33	1.44	11.39	6.49	5.13
S0329a	1.31	1.31	1.21	2.46	1.95	2.08
S0327c	1.53	1.59	1.58	4.87	3.78	3.46
S0327b	1.26	1.37	1.33	1.99	1.70	1.49
S0327a	1.03	1.06	0.93	2.13	1.88	1.86
S0325e	1.16	1.13	1.16	1.53	1.58	1.31
S0325c	1.17	1.16	1.13	2.09	1.48	1.50
S0325b	1.28	1.29	1.38	3.76	2.79	2.90
S0324e	1.29	1.10	1.05	2.07	1.79	1.55
S0324d	1.19	1.20	1.35	1.54	1.58	1.55
S0324c	1.40	1.17	1.23	2.15	1.96	1.72
S0324b	1.22	1.20	1.12	2.19	1.35	1.37
S0324a	1.34	1.42	1.19	1.82	1.46	1.57
S0323c	1.27	1.30	1.21	2.01	1.92	1.72
S0323b	1.33	1.33	1.29	2.11	1.68	1.66
S0323a	1.19	1.17	1.31	2.84	2.64	2.09
S0322a	1.22	1.32	1.20	2.72	2.11	1.82
S0321a	1.29	1.24	1.22	1.70	1.86	1.48
S0320a	1.28	1.30	1.35	3.68	2.67	2.22
S0319b	1.44	1.50	1.56	4.92	3.75	3.19
S0319a	1.03	1.09	1.12	2.72	2.27	2.00
S0318a	1.13	1.12	1.10	2.33	2.01	2.10
S0315d	1.18	1.06	1.20	1.75	1.67	1.59
S0315c	1.10	1.07	1.06	1.40	1.31	1.33
S0315b	1.39	1.44	1.57	2.85	2.11	2.27
S0315a	1.12	1.23	1.20	2.21	1.52	1.55
S0314b	1.28	1.33	1.31	4.97	4.08	3.38
S0314a	1.61	1.40	1.59	2.57	2.20	2.07
S0313a	1.05	1.01	1.01	3.21	2.48	1.99
S0312b	1.26	1.40	1.40	1.97	1.63	1.76
S0312a	1.17	1.29	1.24	1.75	1.55	1.46
S0311b	1.24	1.24	1.18	2.71	2.31	1.90
S0311a	1.53	1.45	1.64	4.65	3.52	3.27
S0310a	1.41	1.47	1.44	2.51	2.16	2.21
S0309c	1.37	1.38	1.37	2.08	1.79	1.76
S0309b	1.23	1.27	1.31	2.11	1.93	1.66
S0309a	1.99	1.34	2.29	2.45	2.42	2.01
S0308a	1.16	1.16	1.16	5.25	4.15	3.12
S0308b	1.77	1.20	1.75	2.76	2.17	2.01
S0306a	1.29	1.32	1.36	3.96	3.23	2.95
S0306c	1.11	1.11	1.19	1.28	1.21	1.13

Event Name	SNRZ LF	SNRN LF	SNRE LF	SNRZ HF	SNRN HF	SNRE HF
S0306d	1.16	1.22	1.33	1.94	1.58	1.47
S0305a	1.19	1.19	1.26	1.46	1.46	1.49
S0304b	1.47	1.45	1.43	4.56	3.45	3.16
S0304a	1.45	1.57	1.54	3.16	2.51	2.09
S0304c	1.28	1.33	1.35	1.92	1.54	1.70
S0303b	1.26	1.17	1.23	2.58	1.60	1.97
S0303a	1.50	1.39	1.38	2.91	2.23	2.26
S0302d	1.18	1.13	1.14	1.38	1.11	1.11
S0302c	1.20	1.20	1.26	1.69	1.48	1.24
S0302b	1.10	1.09	1.28	1.56	1.39	1.32
S0302a	1.30	1.26	1.32	1.98	1.72	1.64
S0301b	1.20	1.20	1.42	1.62	1.41	1.53
S0301a	1.30	1.27	1.10	2.81	1.93	1.79
S0300a	1.12	1.26	1.26	2.17	1.77	1.73
S0299b	1.24	1.28	1.27	2.18	1.83	1.69
S0299a	1.23	1.32	1.34	3.57	2.70	2.14
S0298a	1.26	1.16	1.25	2.26	1.49	1.44
S0297e	1.17	1.19	1.20	1.57	1.48	1.46
S0297d	1.09	1.11	1.01	1.29	1.13	1.06
S0297c	1.37	1.31	1.20	2.18	1.76	1.69
S0297b	1.26	1.26	1.24	1.92	1.60	1.50
S0297a	1.57	1.26	1.27	3.26	2.33	2.15
S0295b	1.11	1.07	1.11	1.84	1.57	1.44
S0295a	1.98	1.99	1.61	2.88	2.26	2.04
S0294b	1.56	1.52	1.49	3.16	2.66	2.37
S0294a	1.09	1.10	1.21	2.17	2.06	1.63
S0292a	1.30	1.32	1.35	3.14	2.78	2.51
S0292c	1.18	1.26	1.23	2.19	2.04	1.63
S0292b	1.20	1.35	1.31	1.56	1.36	1.48
S0291a	1.30	1.34	1.28	3.21	2.39	1.88
S0290a	1.46	1.17	1.22	2.14	1.76	1.54
S0265e	1.30	1.22	1.26	1.77	1.41	1.37
S0265d	1.28	1.17	1.26	1.90	1.97	1.82
S0265c	1.29	1.32	1.48	1.44	1.31	1.35
S0265b	1.53	1.63	1.66	2.10	1.80	1.55
S0265a	1.25	1.16	1.07	1.73	1.85	1.45
S0264d	1.14	1.18	1.19	1.66	1.44	1.29
S0264c	1.30	1.32	1.29	1.39	1.39	1.36
S0264b	1.48	1.48	1.58	2.50	2.07	1.80
S0261b	1.22	1.18	1.18	2.45	2.20	2.24
S0261a	1.43	1.36	1.40	2.09	1.74	1.58
S0260b	1.23	1.20	1.40	1.75	1.60	1.42
S0260a	2.01	1.87	2.09	6.99	5.42	4.72
S0257c	1.04	1.23	0.99	1.35	1.51	1.30
S0257b	1.37	1.29	1.31	2.71	3.42	2.57

Event Name	SNRZ LF	SNRN LF	SNRE LF	SNRZ HF	SNRN HF	SNRE HF
S0257a	1.77	1.47	1.55	2.29	2.73	2.23
S0256c	1.20	1.27	1.17	1.67	1.67	1.64
S0256a	1.14	1.17	1.21	1.86	1.66	1.50
S0256b	1.21	1.21	1.11	1.76	1.35	1.23
S0255b	1.42	1.18	1.31	2.33	2.19	1.70
S0255a	1.15	1.33	1.34	1.30	1.30	1.14
S0254c	1.25	1.18	1.20	1.70	1.78	1.56
S0254a	1.16	1.40	1.47	2.17	1.93	1.51
S0253b	1.17	1.15	1.23	1.45	1.37	1.33
S0253a	1.08	1.23	1.09	1.76	1.38	1.54
S0252a	1.32	1.20	1.27	2.91	2.89	2.26
S0252b	1.44	1.42	1.24	2.12	1.76	1.75
S0251c	1.12	1.43	1.55	1.71	1.44	1.39
S0251b	1.16	1.34	1.38	1.36	1.60	1.36
S0250b	1.24	1.27	1.18	1.40	1.36	1.27
S0250a	1.14	1.54	1.35	1.49	1.36	1.49
S0249a	1.14	1.13	1.14	1.52	1.55	1.63
S0248b	1.14	1.12	1.20	1.66	1.62	1.44
S0248a	1.26	1.17	1.33	2.17	1.74	1.61
S0248c	1.29	1.24	1.24	1.74	1.36	1.30
S0247b	1.22	1.20	1.15	1.60	1.63	1.27
S0247a	1.19	1.22	1.16	2.04	1.84	1.84
S0244d	1.23	1.49	1.36	2.28	1.75	1.84
S0244e	1.18	1.13	1.16	1.41	1.20	1.11
S0244c	1.19	1.15	1.18	1.95	1.65	1.49
S0244b	1.10	1.25	1.20	1.52	1.28	1.34
S0244a	1.05	0.94	1.09	1.33	1.24	1.22
S0242d	1.21	1.21	1.11	1.24	1.09	1.09
S0242b	1.35	1.30	1.27	1.71	1.81	1.42
S0242a	1.63	1.41	1.63	2.73	2.37	2.05
S0242c	1.28	1.20	1.29	3.10	2.26	1.95
S0241b	1.40	1.39	1.30	1.37	1.41	1.29
S0241a	1.12	1.37	1.23	1.58	1.37	1.19
S0239a	1.75	1.68	1.83	4.45	3.32	3.06
S0238a	1.01	1.31	1.15	1.35	1.25	1.27
S0237a	1.13	1.04	1.09	1.41	1.34	1.29
S0236b	1.28	1.20	1.21	1.47	1.35	1.21
S0236a	1.12	1.39	1.28	1.80	1.57	1.42
S0235d	1.32	1.29	1.17	1.52	1.68	1.82
S0235a	1.08	1.09	1.20	1.55	1.42	1.30
S0234b	1.18	1.09	1.03	1.51	1.48	1.27
S0234a	1.22	1.07	1.23	2.98	1.97	1.86
S0229a	1.16	1.15	1.10	2.14	1.80	1.72
S0228c	1.40	1.44	1.45	3.21	3.11	2.39

Event Name	SNRZ LF	SNRN LF	SNRE LF	SNRZ HF	SNRN HF	SNRE HF
S0228b	1.12	1.37	1.28	1.57	1.55	1.41
S0228a	1.04	1.40	1.18	1.42	1.35	1.25
S0227d	1.30	1.17	1.27	2.37	1.93	2.01
S0227c	1.26	1.23	1.24	2.39	1.76	1.65
S0227b	1.08	1.02	1.10	1.27	1.05	1.02
S0227a	1.17	1.28	1.23	1.30	1.22	1.02
S0226c	1.14	1.05	1.07	1.48	1.51	1.37
S0226a	1.07	1.17	1.33	1.44	1.44	1.47
S0225a	1.25	1.34	1.16	1.60	1.42	1.46
S0222a	1.21	1.39	1.31	2.53	2.13	1.72
S0221c	1.02	0.97	1.09	1.44	1.36	1.37
S0221b	1.04	1.14	1.14	1.39	1.51	1.47
S0221a	1.34	1.29	1.13	3.42	2.31	2.01
S0219c	1.20	1.23	1.18	2.39	2.08	1.64
S0219b	1.13	1.13	1.10	2.39	2.10	2.03
S0219a	1.15	1.30	1.14	1.67	1.71	1.82
S0218a	1.20	1.05	1.21	3.51	2.58	1.90
S0216b	1.08	0.99	0.98	2.28	1.95	1.87
S0215b	1.05	1.11	1.12	1.29	1.00	1.17
S0215a	1.24	1.21	1.24	1.60	1.35	1.34
S0213a	1.15	1.29	1.20	2.36	1.95	1.75
S0212c	1.35	1.31	1.25	2.18	1.71	1.77
S0212b	1.35	1.25	1.19	2.47	1.97	2.08
S0212a	1.33	1.14	1.20	1.89	1.92	1.80
S0211a	1.19	1.21	1.25	2.15	1.65	1.63
S0211b	1.19	0.98	1.04	1.97	1.46	1.41
S0204a	1.22	1.00	1.12	1.99	1.78	1.44
S0203b	1.14	1.09	1.15	1.76	1.50	1.31
S0203a	1.19	1.18	1.13	1.53	1.40	1.32
S0202c	1.11	1.19	1.22	3.86	2.76	2.64
S0202b	1.16	1.17	1.07	3.12	2.24	1.92
S0202a	1.42	1.06	1.08	1.99	1.61	1.52
S0201b	1.20	1.13	1.17	2.83	2.07	2.12
S0200a	1.16	1.15	1.12	2.31	1.78	1.61
S0197a	1.15	1.14	1.13	1.39	1.52	1.31
S0194d	1.11	0.97	1.08	2.39	1.85	1.81
S0194c	1.14	1.14	1.27	2.11	1.49	1.66
S0194b	1.07	0.94	1.05	1.61	1.50	1.41
S0194a	1.06	1.31	1.15	1.60	1.70	1.45
S0193a	0.97	1.03	0.95	1.52	1.30	1.39
S0191a	0.97	1.01	1.10	1.58	1.55	1.36
S0186a	0.94	0.98	0.96	1.14	1.08	1.15
S0186b	1.03	1.07	1.00	1.47	1.30	1.11
S0185b	1.38	1.25	1.32	2.33	2.01	1.63
S0183b	1.32	1.47	1.35	1.58	1.69	1.46
S0168a	1.37	1.33	1.30	1.59	1.36	1.23
S0166a	1.24	1.38	1.22	6.24	5.17	4.14